

# Siah2 antagonism of Pard3/JamC modulates Ntn1-Dcc signaling to regulate cerebellar granule neuron germinal zone exit

Received: 2 July 2022

Accepted: 11 December 2024

Published online: 07 January 2025

 Check for updatesChristophe Laumonnerie<sup>1</sup>, Maleelo Shamambo<sup>1</sup>, Daniel R. Stabley<sup>1</sup>, Tommy L. Lewis Jr<sup>2</sup>, Niraj Trivedi<sup>1</sup>, Danielle Howell<sup>1</sup> & David J. Solecki<sup>1</sup>✉

Exiting a germinal zone (GZ) initiates a cascade of events that promote neuronal maturation and circuit assembly. Developing neurons and their progenitors must interpret various niche signals—such as morphogens, guidance molecules, extracellular matrix components, and adhesive cues—to navigate this region. How differentiating neurons in mouse brains integrate and adapt to multiple cell-extrinsic niche cues with their cell-intrinsic machinery in exiting a GZ is unknown. We establish cooperation between cell polarity-regulated adhesion and Netrin-1 signaling comprises a coincidence detection circuit repelling maturing neurons from their GZ. In this circuit, the Partitioning defective 3 (Pard3) polarity protein and Junctional adhesion molecule-C (JamC) adhesion molecule promote, while the Seven in absentia 2 (Siah2) ubiquitin ligase inhibits, Deleted in colorectal cancer (Dcc) receptor surface recruitment to gate differentiation linked repulsion to GZ Netrin-1. These results demonstrate cell polarity as a central integrator of adhesive- and guidance cues cooperating to spur GZ exit.

During nervous system development, sequential events ensure the formation of the neuronal circuitry required for proper cognitive function. At the cellular level, maturing neurons navigate multifaceted tissue environments by interpreting cell-extrinsic factors that cooperate with cell-intrinsic programs to bring about the stereotypical progression of cells from neuronal progenitors to mature neurons with proper identity, location, and connectivity<sup>1</sup>. Flawed execution of these genetically encoded but environmentally regulated programs has drastic consequences for brain morphogenesis and circuit function, and it ultimately leads to a wide range of pediatric neurological disorders<sup>2</sup>. There is compelling evidence that extrinsic factors, such as guidance molecules and intrinsic programs, such as those involving neuronal polarity signaling or cytoskeletal organization, are important for germinal zone (GZ) exit, migration, and synaptogenesis in circuit formation. However, understanding how cell biological programs like neuronal polarity signaling coordinate with extrinsic guidance signals

remains a significant challenge due to a reductionist focus on how molecular players function in isolation and a lack of cell biological or imaging approaches to tackle this issue mechanistically. This study addresses this challenge by revealing how cell polarity signaling, cell adhesion, and the sensing of guidance molecules work in unison at the cell biological level to control when neuronal progenitor cells or newly differentiated neurons leave their germinal niche.

Granule neurons from the mouse cerebellar cortex have long been a system of choice for studying the process whereby neuronal progenitor replication in proliferative niches transitions to differentiation of neurons that migrate out of their GZ to a final laminar position<sup>3–5</sup>. In the outer external granule layer (oEGL), granule neuron progenitors (GNPs) exhibit a low-polarity morphology. As they differentiate, newborn cerebellar granule neurons (CGNs) progressively extend a leading process parallel to the surface of the cerebellar cortex and start migrating along that axis in the inner external granule layer

<sup>1</sup>Neuronal Cell Biology Division, Department of Developmental Neurobiology, St. Jude Children's Research Hospital, 262 Danny Thomas Place, Memphis, TN 38104, USA. <sup>2</sup>Aging & Metabolism Program, Oklahoma Medical Research Foundation, 825 NE 13th Street, Oklahoma City, OK 73104, USA.

✉ e-mail: [david.solecki@stjude.org](mailto:david.solecki@stjude.org)

(iEGL). Eventually, CGNs extend a perpendicular process, and the soma starts migrating radially on the surface of Bergmann glia fibers to reach the inner granule layer (IGL), leaving the axon behind in the molecular layer. This model is ideal for understanding how disparate cell biological processes act in unison. Recent work has shown that transcriptional and post-transcriptional regulation of polarity complex protein availability is critical for GZ exit. GNPs express the E3 ubiquitin ligase Siah2, which targets Pard3 for degradation<sup>6</sup>. Additionally, hypoxic pressure in the GZ and expression of the transcription factor Zeb1 transcriptionally repress Pard6 $\alpha$  and Pard3 mRNA expression, thus maintaining cells in the EGL<sup>7,8</sup>. As CGNs differentiate, the loss of transcriptional and post-translational repression, marked by diminished expression of Siah2 and Zeb1, leads to the expression of polarity proteins. This change enables one neurite to specialize as a leading process, promoting the recruitment of junctional adhesion molecule type C (JamC) to the cell surface<sup>6</sup>. Consequently, JamC facilitates adhesion to radial glial fibers, providing a substrate for migration through the molecular layer<sup>9–11</sup>. Despite the well-developed role of this polarity-dependent adhesion system in GZ exit, we still do not understand how this critical pathway is linked to classical guidance molecules that could functionally align cellular asymmetry to external reference points as newborn neurons take up their positions in the cerebellar circuit.

A large array of extrinsic cues have been identified as making short-range and long-range contributions to the cell cycle regulation of GNPs and the migration of CGNs<sup>5</sup>. This myriad of signals raises the question of how a given neuron can filter out only those cues relevant to its behavior at a given time. We hypothesized that cellular polarization and polarity complex proteins could modulate the strength of extrinsic guidance signals by regulating the access of transmembrane receptors to the membrane surface. To test this idea, we investigated the function of the guidance molecule netrin-1 (Ntn1) in guiding CGNs out of the GZ. Ntn1 signaling is transduced by different transmembrane receptors of the immunoglobulin superfamily, like the deleted in colorectal cancer (Dcc) and Uncoordinated protein 5 (Unc5) transmembrane proteins, and is involved in axonal guidance and neuronal migration<sup>12–15</sup>. Based on the combination of receptors expressed by the cell, the signal can mediate attraction or repulsion behavior<sup>15</sup>. Although Ntn1 is not known to guide the migration of GNPs from the upper rhombic lip in the cerebellar system, postnatal cerebellar cortex explants showed that Ntn1 repelled parallel fiber extensions; however, the function of neither Dcc nor Unc5 receptors were formally assessed at the time<sup>16</sup>. In addition, the mutant model for another Ntn1 receptor, Unc5c, has been described as possessing a smaller cerebellum and folia, ectopic cerebellar cells in the midbrain, and abnormal postnatal cerebellar migration<sup>12</sup>.

In this study, we used the GZ exit of differentiating CGNs in the cerebellum as a model to study how extracellular guidance cue–receptor pairs, such as Dcc and Ntn1, a cellular polarity complex, and an adhesion protein can intersect, creating a coincidence detection circuit that modulates cellular migration. Our results reveal a localized source of Ntn1 in the EGL, where GNPs reside, and Unc5c upregulation promotes GZ exit, specifically of newly differentiated CGNs. Levels of Dcc receptors were found to be critical for tuning the sensitivity of the response. Using FACS-sorted populations of GNPs and CGNs, we show that differentiated neurons migrate away from a source of Ntn1, whereas progenitors show no preferential migration orientation. These observations led us to investigate how the access of transmembrane receptors to the membrane surface was regulated. Like Pard3, Dcc has been previously reported to be targeted for degradation by the proteasome by Siah proteins<sup>17–19</sup>. Here we show that Siah2 promotes GZ occupancy by decreasing the amount of Dcc receptors at the membrane. Using super-resolution microscopy, we provide evidence that Dcc receptors reside near Pard3 and JamC at the membrane surface; additionally, a proximity labelling assay (PLA)

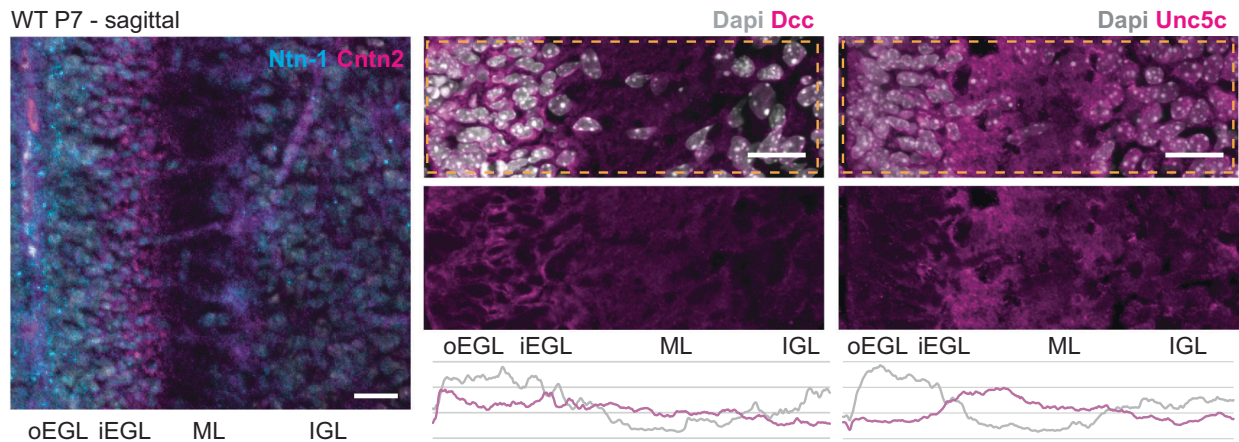
shows that JamC, Pard3, and Dcc form a protein complex. We demonstrate that Pard3 and JamC functions are essential to a proper Ntn1-mediated migration phenotype in an ex vivo assay. Necessity–sufficiency testing revealed that Pard3 promotes Dcc receptor clustering in response to netrin-1, whereas JamC controls the basal levels of Dcc at the surface. Thus, Pard3 and JamC regulate the sensitivity of newly differentiated CGNs to the netrin gradient by adjusting the number of Dcc receptors recruited to the cell surface. This paradigm for cooperativity between disparate cell biological processes illustrates that coincidence detection between JamC and polarity-dependent adhesion and sensitivity to a repulsive netrin-1 work in tandem to facilitate GZ exit, with the polarity pathway concentrating Dcc at cell surface locations by stabilizing and/or promoting transmembrane receptor exocytosis. Siah2 ubiquitin ligase activity antagonizes these complexes via ubiquitin-based turnover, thus favoring progenitor GZ occupancy.

## Results

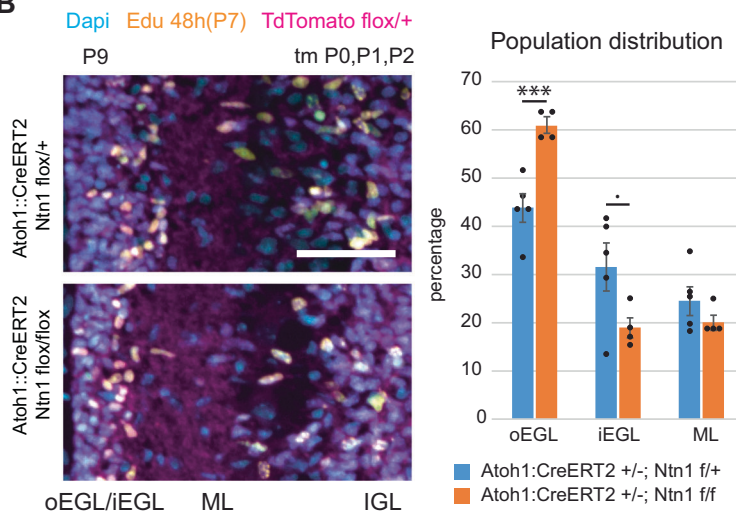
Ntn1 signaling has been implicated in guiding early aspects of cerebellar morphogenesis, such as repulsion of CGN axons and the positioning of the boundary of the forming EGL<sup>12,16</sup>, making it an excellent guidance molecule model for assessing cooperativity with polarity proteins. While their mRNA expression was analyzed previously, we reassessed the expression of Ntn1 and its receptors Dcc and Unc5c at the protein level in postnatal day 7 (P7) mice. Immunohistochemical staining revealed that Ntn1 is present in the oEGL complementary to Cntn2 CGN marker expression in the iEGL. In contrast, immunohistochemical staining for Ntn1 receptors showed that Dcc and Unc5c are expressed strongly in the iEGL. Whereas Dcc expression is also in the oEGL, especially close to the Pia, Unc5c appears more restricted to the iEGL and ML (Fig. 1A). Unc5c's restricted expression pattern was surprising as previous analyses of its mRNA expression showed expression in all cerebellar layers. These expression patterns suggest that Ntn1 and its receptors are well-positioned to affect CGN GZ exit and/or layer occupancy decisions at the transition zone between iEGL and ML.

We next assessed whether Ntn1 function affected GZ exit in the developing cerebellum in vivo by using a Cre-inducible system to generate *Atoh1::CreERT2/Ntn1<sup>lox/lox</sup>; Rosa::TdTomato<sup>lox/ut</sup>* mice, as this has not been done in previous studies. In vivo GZ pulse-chase analysis was conducted in animals to whom tamoxifen was administered daily from P0 to P3, using one dose of 5-ethynyl-2'-deoxyuridine (EdU) injected at P7. The EdU GZ pulse labels the proliferative GNPs of the oEGL in the cerebellar cortex when injected at P7. The position of Edu/TdTomato-positive cells in tissues collected at later stages of development can be used as a proxy to analyze the GZ exit and migration of the CGN progeny of GNPs in vivo. At P9, the average distance from the cerebellar surface of Edu/TdTomato-positive nuclei, which is a measure of GZ exit and subsequent migration, was lower in *Atoh1::CreERT2/Ntn1<sup>lox/lox</sup>; Rosa::TdTomato<sup>lox/ut</sup>* mice than in their *Atoh1::CreERT2/Ntn1<sup>lox/WT</sup>; Rosa::TdTomato<sup>lox/ut</sup>* littermates, showing that deleting Ntn1 from the EGL results in the inhibition of GZ exit (Fig. 1B). Given that Ntn1 has been previously described as an oncogene, limiting apoptosis induced by its receptors Dcc and Unc5c<sup>20</sup>, we assessed proliferation and apoptosis status. In antibody staining experiments on wild-type and mutant animals, we denoted EGL subdivisions using Cntn2 immunostaining: iEGL (Cntn2 positive) and oEGL (Cntn2 negative), along with the actively cycling neuronal progenitor marker Ki67 and the apoptosis marker Cleaved-Caspase3. The results showed no differences between WT and knock-down animals at this developmental stage (Fig. S1A, B). Additionally, dissociated CGN cultures supplemented with Ntn1 demonstrated a significant reduction in the proportion of progenitor cells after 48 h of culture (Fig. S1C), indicating that Ntn1 does not directly maintain proliferation. Therefore, the increased EGL occupancy of Edu-labeled neurons observed in the Ntn1 knockdown of the *Atoh1* lineage (Fig. 1B) is likely due to a migratory defect.

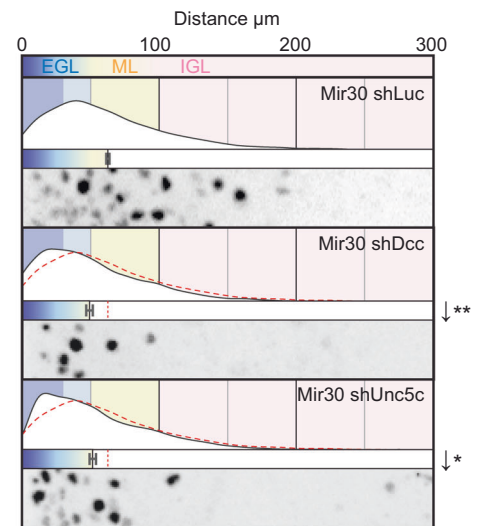
**A**



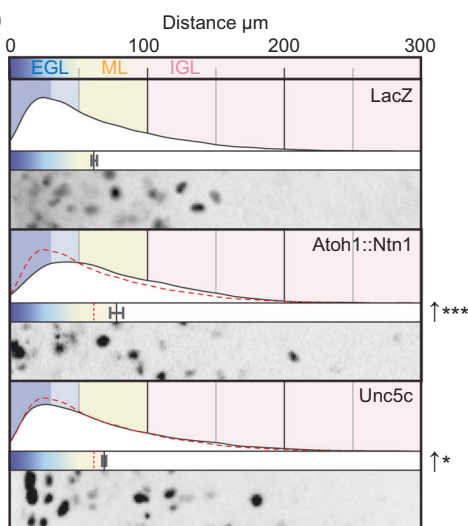
**B**



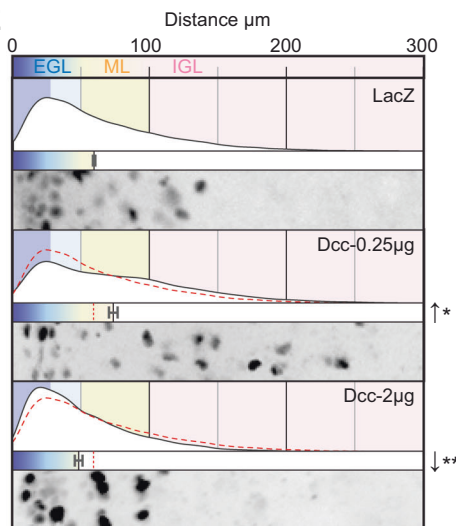
**C**



**D**



**E**



Given the expression of Dcc and Unc5c in differentiated CGNs, we next assessed the function of these receptors in GZ exit by using the ex vivo slice culture assay developed in our laboratory, as the functional role of these receptors has not been assessed in the CGN lineage. Silencing of either Unc5c or Dcc via Mir30 shRNA expression significantly reduced the average radial migration distance from the pial surface after 48 h in culture and increased the proportion of cells that remained in the EGL (Fig. 1C). These results are consistent with studies

showing that Dcc/Unc5 heterodimers mediate chemorepulsion from a source of Nnt1<sup>15</sup>, buttressing our finding that Ntn1 loss of function led to enhanced GZ occupancy. Interestingly, the average migration speed was not affected by Dcc and Unc5c silencing in dissociated CGN cultures (Fig. S1D), showing that the loss of GZ exit in silenced cells is not due to defective cell motility.

Given the necessity of Ntn1, Dcc, and Unc5c for CGNs to take up positions outside the EGL, we next tested whether they were sufficient

**Fig. 1 | Expression of Ntn1 system components and their manipulation in vivo and ex vivo affects GZ occupancy.** **A** Immunohistochemical staining of sagittal cryo-sections of wild-type and Atoh1-GFP mouse cerebella at P7. From left to right, the sections were stained using antibodies against Ntn1 (cyan) and Cntn2 (magenta), Dcc (magenta), and Unc5c (magenta), and were counterstained with Dapi (white). Dashed-line boxes highlight regions used for average intensity plot over the radial axis. **B** Sagittal cryo-sections through the cerebella of P9 Rosa::Td-Tomato<sup>fl/+</sup>; Atoh1::CreERT2<sup>+/-</sup>; Ntn1<sup>flox/wt</sup> ( $n = 5$ ) or Ntn1<sup>flox/flox</sup> ( $n = 4$ ) animals after three doses of tamoxifen (tm) at P0, P1, and P2 and a single injection of Edu at P7. Sections were stained for Edu, and the radial distance from the edge of the Edu<sup>+</sup> nucleus was measured and plotted. oEGL: 0–30  $\mu\text{m}$ ; iEGL: 30–50  $\mu\text{m}$ ; ML: 50–100  $\mu\text{m}$ . **C–E** Results of ex vivo slice culture assays under different conditions. In each case, the top curve shows the entire distribution of the radial distances of H2B-positive electroporated nuclei from the edge of the slice in replicates. Below this is a plot of the average radial distance from the edge among replicates, and below this

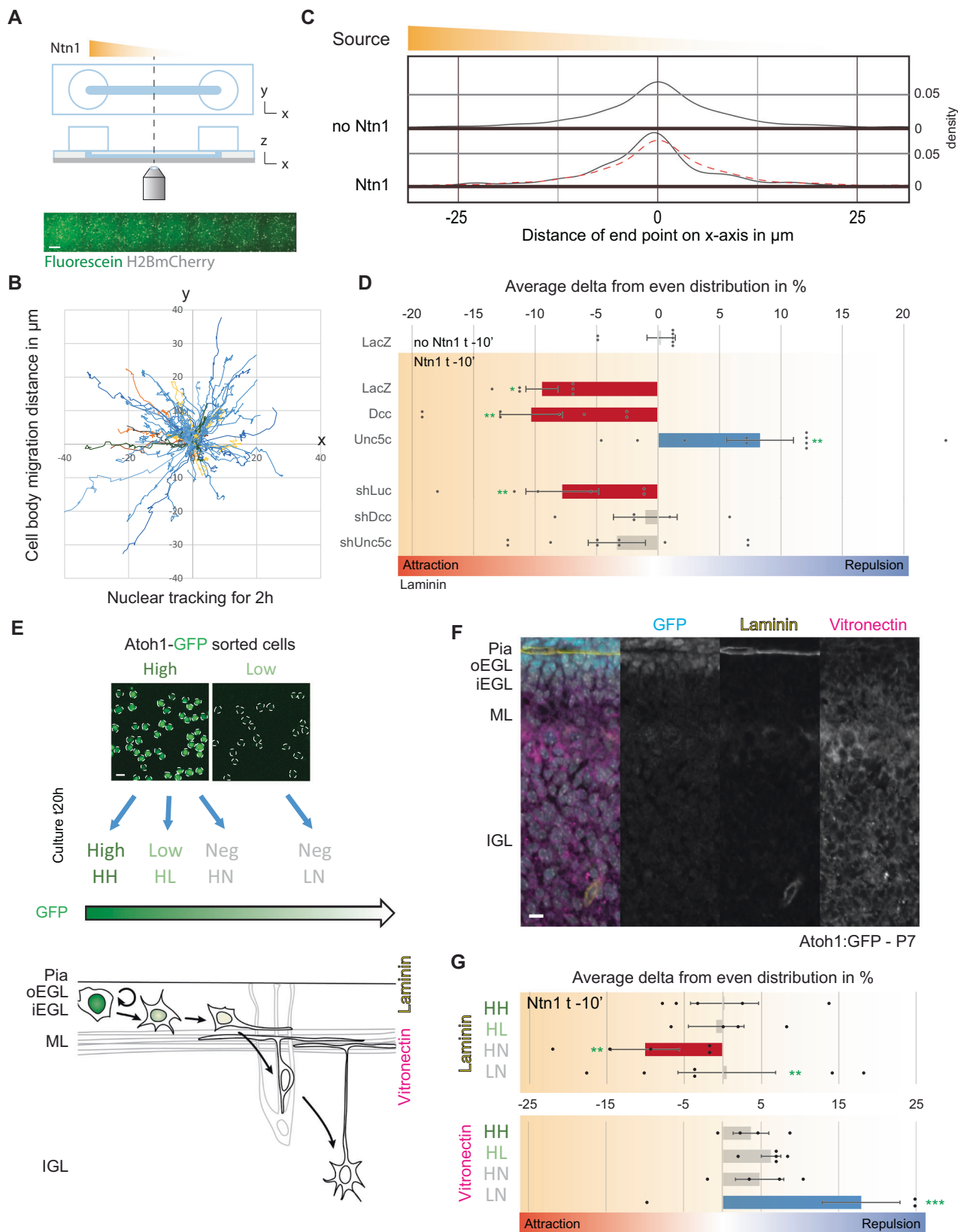
is a micrograph representative of the nuclear distribution in that assay. All are displayed on the same scale, representing a distance from 0 to 300  $\mu\text{m}$ . In addition to H2B-Cherry, the following constructs were electroporated: in (C), Mir30 shLacZ (control,  $n = 4$ ), Mir30 shDcc ( $n = 5$ ) and Mir30 shUnc5c ( $n = 3$ ); in (D), LacZ (control,  $n = 5$ ), Atoh1::Ntn1 ( $n = 4$ ), and Unc5c ( $n = 5$ ); in (E), LacZ (control,  $n = 5$ ), Dcc at 0.25  $\mu\text{g}$  ( $n = 5$ ), and Dcc at 2  $\mu\text{g}$  ( $n = 4$ ). Each respective control is represented by a red dashed line in the distribution plot. Scale bars in (A) and (B) represent 20  $\mu\text{m}$  and 50  $\mu\text{m}$ , respectively. Abbreviations: oEGL, outer external granule layer; iEGL, inner external granule layer; EGL, external granule layer; ML, molecular layer; IGL, internal granule layer. In (B) through (E), the error bars represent the SEM. Statistics: \* $p \leq 0.05$ ; \*\* $p \leq 0.01$ , \*\*\* $p \leq 0.005$ , as assessed by a Student t-test (one-sided, unpaired) in (B) and an ANOVA followed by a Dunnett post hoc test in (C–E) against the respective controls. See also Source Data File. Scale bars in (A) and (B) represent 20  $\mu\text{m}$  and 50  $\mu\text{m}$ , respectively.

to induce GZ exit. Expressing Ntn1 in ex vivo slices by using the Atoh1 regulatory sequence to restrict its expression to the oEGL increased the average radial distance of electroporated nuclei from the pial surface and reduced EGL occupancy (Fig. 1D). Elevated expression of Unc5c, which is expressed only as CGNs differentiate, resulted in a similar precocious GZ exit phenotype (Fig. 1D). Expression of Dcc exhibited a concentration-specific phenotype: a mild elevation of Dcc expression promoted GZ exit, whereas at higher concentrations, cells remained in the GZ (Fig. 1E). This phenotypic transition was gradual (Fig. S1E) and, based on the literature, could reflect the fact that increasing the number of Dcc receptors at the cell surface favors Dcc homodimer formation and attraction to a source of Ntn1<sup>15,21</sup>, whereas when the number of Dcc receptors is low, they may cooperate with endogenous Unc5, promoting repulsion. These results show that Dcc expression and the regulation of its availability at the membrane surface appear to be critical to modulating the GZ exit response to Ntn1 in the oEGL.

To assess whether Ntn1 signaling directly affected CGN migration direction, we used an in vitro system to control the source of this guidance cue. Channel microslides can set and hold a gradient for several hours, enable different substrate coatings to be placed on the glass base of the slide, and are optically compatible with time-lapse microscopy. Dissociated cerebellar neurons were nucleofected and seeded into the channel of a microslide and incubated for 24 h. Ten minutes before the start of an imaging experiment, the medium in the channel was replaced, and that in the left half of the slide was replaced with medium containing 200 ng/mL of recombinant Ntn1 or its equivalent in volume in 1 $\times$  PBS as a control. Fluorescein was also added to enable visualization of the gradient status over time (Fig. 2A). The motion of H2b-mCherry-labeled nuclei in the middle of the channel was assayed via 2 h of live-cell time-lapse microscopy followed by computational tracking of nuclei to determine the cell response to an oriented Ntn1 source (Fig. 2B). For simplicity, we expressed the tracking results as variations from a 50%:50% distribution in the x-axis of the slide, as there were no specific alterations in the relative endpoint displacement in the gradient y axis. Although the endpoint distribution of migration on the x-axis showed no preferential direction in control cells, exposure to the Ntn1 gradient resulted in an attractive shift toward the source of Ntn1 (Fig. 2C). A chi-square statistical test revealed that the pattern of attraction observed with Ntn1 was significantly different from a 50%:50% distribution (Fig. 2D). To validate the dependency of migration on Ntn1 signaling, we nucleofected constructs to modify the expression levels of the Ntn1 receptors. On laminin-coated slides, a gain of function of Dcc maintained the attraction phenotype observed in controls, whereas the gain of function of Unc5c reversed the phenotype to a repulsive one, with cells migrating away from the source of Ntn1 (Fig. 2D). Mir30-based shRNA knockdown of both *Dcc* and *Unc5c* mRNA resulted in the loss of responsiveness to the source of Ntn1 (Fig. 2D). We should note that

shUnc5c trended towards attraction, but experimental variability rendered the  $p$ -value of the Chi-squared statistical test above the 0.05 level. However, this result is still consistent with a loss of GZ exit for Unc5c deficient CGNs in the cerebellar slice assay. Overall, these results confirm that the Ntn1 receptors Dcc and Unc5c are essential to reorienting somal migration of dissociated CGNs in response to a source of Ntn1.

Given the differentiation-specific expression of Dcc and Unc5c, we were curious as to whether GNPs and CGNs at various differentiation stages had distinct responses to Ntn1. We took advantage of the knock-in mouse line in which EGFP is fused in-frame with the Atoh1 transcription factor that is expressed specifically in GNPs (Fig. 2E). Atoh1-EGFP fluorescence had two uses in our experiment: 1) Atoh1-EGFP fluorescence could be used to sort dissociated EGL cells into GNPs (Atoh1-high, Pax6<sup>+</sup>) and CGNs (Atoh1-low, Pax6<sup>+</sup>) (Fig. S2A), with Atoh1-negative cells from the initial sort being in majority Pax2<sup>+</sup> interneurons (Fig. S2B); and 2) the intensity of Atoh1-EGFP in time-lapse imaging assays reported the differentiation status of the purified CGN lineage cells in real-time. In the Ntn1 migration assay, Atoh1-high and Atoh1-low populations were plated on microslides 24 h before time-lapse imaging of their response. We also coated microslides with extracellular matrix components that are enriched near the oEGL (laminin) or iEGL (vitronectin) to better recapitulate conditions near the EGL niche (Fig. 2F). Our time-lapse imaging revealed that the Atoh1-high population maintained a high level of Atoh1-GFP (true GNPs; designated HH cells), transitioned to a low level of Atoh1-GFP (intermediate GNPs; designated HL cells), or lost Atoh1-GFP altogether (recently differentiated CGNs; designated HN cells) (Fig. 2E). Cells from the “low” sorted population remained negative for Atoh1-GFP and represented more mature CGNs (designated LN cells in Fig. 2E). On both substrates, the HH and HL populations of Atoh1-GFP-positive cells showed no significant directional bias when migrating in the Ntn1 gradient (Fig. 2G). On laminin, the HN population of newly differentiated CGNs migrated significantly toward the source of Ntn1 but showed no preference on vitronectin (Fig. 2G). Conversely, the LN population of more mature CGNs migrated away from the Ntn1 source on vitronectin, which mimics the extracellular matrix components in the iEGL and the molecular layer. The behavior of the LN population on laminin was heterogeneous. A comparison to an even distribution with a chi-square test (Fig. 2G) revealed that some cells had an attraction response (Fig. S2C, magenta arrowhead) whereas others had a strong repulsion response (Fig. S2C, cyan arrowhead), indicating that HL cells exposed to laminin could have a slower transition from attraction to repulsion. It is worth noting that vitronectin promotes CGN differentiation<sup>22,23</sup>, whereas laminin, in some contexts, maintains GNPs and CGNs in an immature state<sup>23,24</sup>. Collectively, our in vivo, ex vivo, and microslide experiments show that the level of Dcc protein is critical for the regulation of GZ exit by Ntn1 signaling (Fig. 1E)



and that GNPs and CGNs display distinct responses to the presence of Ntn1 in the EGL GZ that differ according to their maturation status (Fig. 2G).

We were intrigued by the differentiation-specific expression of Dcc in CGNs and that Dcc expression levels modulated the response to Ntn1 in the ex vivo cerebellar slice assay. Accordingly, we assessed how Dcc

levels were controlled during CGN differentiation. Previous work from our laboratory has shown that Siah2 (seven in absentia homolog 2), a Ring-domain E3 ubiquitin ligase, is strongly expressed in GNPs and that it regulates GZ occupancy by targeting for degradation key proteins of the polarity complex, primary cilia, and hypoxia pathway<sup>6,8,23,24</sup>. Furthermore, we show here that Siah2 expression decreases in tandem

**Fig. 2 | The CGN lineage has differential Ntn1 responses depending on differentiation status and cell extrinsic signals.** **A** Schematic of channel microslides used to assess cerebellar granule neuron (CGN) migration in response to unilateral Ntn1 addition, visualized by time-lapse imaging. Tiled images show dissociated CGNs, nucleofected with H2B-mCherry (white), within a fluorescein gradient (green) formed in the center of the channel. **B** Manual tracking of nuclear motion over a 2 h time-lapse session without Ntn1, with the x-axis aligned with the channel. **C** Endpoint displacements distribution along the x-axis for migration in the “no Ntn1” (red dashed line,  $n = 338$ ) and with unilateral Ntn1 addition on the left ( $n = 379$ ). Ntn1 gradient was applied 10 min before imaging. **D** Chart of average variation in endpoint nuclear displacement from a 50%:50% even probability, indicating attraction (negative values, in red if significant) or repulsion (positive values, in blue if significant). CGNs were plated on laminin-coated microslides and incubated 24 h before imaging, with Ntn1 gradient applied 10 min before 2 h time-lapse nuclear tracking. Cells were nucleofected with H2B-mCherry, GPI-pHluorin, and various conditions: LacZ (without Ntn1  $n = 6$ , +Ntn1  $n = 6$ ), Dcc ( $n = 8$ ), Unc5c

( $n = 10$ ), shLuc ( $n = 6$ ), shDcc ( $n = 5$ ), or shUnc5c ( $n = 10$ ). **E** Top: Dissociated CGNs from Atoh1-GFP mice, sorted by high and low GFP intensity (green). Bottom: Schematic of cerebellar layers in P7 Atoh1-GFP mice, showing the decrease in GFP intensity during GNP differentiation and migration from the oEGL to the IGL, with a shift from laminin-diff to vitronectin-rich extracellular matrix.

**F** Immunohistochemistry of P7 Atoh1-GFP cerebellum showing GFP (cyan), laminin (yellow), and vitronectin (magenta) staining in sagittal cryo-sections. **G** Chart of average variation in endpoint nuclear displacement as described in **(D)** for FACS-sorted Atoh1-GFP neurons plated on laminin- (HH:  $n = 5$ ; HL:  $n = 4$ ; HN:  $n = 5$  and LN:  $n = 6$ ) or vitronectin-coated (HH:  $n = 4$ ; HL:  $n = 5$ ; HN:  $n = 4$  and LN:  $n = 4$ ) microslides with unilateral Ntn1 addition. Scale bars: **(A)** 100  $\mu\text{m}$ , **(E)** and **(F)** 10  $\mu\text{m}$ . Abbreviations: oEGL outer external granule layer, iEGL inner external granule layer, EGL external granule layer, ML molecular layer, IGL internal granule layer. In **(D)** and **(G)**, error bars represent SEM. Statistics:  $*p \leq 0.05$ ,  $**p \leq 0.01$ ,  $***p \leq 0.005$ , via chi-square test against an even 50%:50% probability. See Source Data File.

with Atoh1-GFP fluorescent signal as CGNs differentiate and start to migrate deeper in the cerebellum (Fig. S3A). Indeed, the sorted cells we used for our channel microslide experiments (e.g., HH, HL, HN, and LN cells defined in the last section) significantly vary in their relative Siah2 expression level in addition to their behavior in a Ntn1 gradient (Fig. 3A). While some synergy exists between Siah2 activity and the mitogenic factor Shh that prevents GNPs from differentiating<sup>24</sup>, Shh does not directly drive *Siah2* mRNA expression in dissociated CGNs culture (Fig. S3B), suggesting a post-transcriptional reduction in CGN differentiation.

The Dcc protein carries the canonical degron motif Pro-X-Ala-X-Val-X-Pro, which is recognized by Siah proteins within its intracellular P2 domain<sup>25</sup> (Fig. 3B). This motif is well conserved in organisms ranging from *Xenopus* to humans (Fig. S3C) and has been shown to promote specific proteasomal degradation of Dcc by Siah proteins<sup>18</sup>. To confirm the specificity of Siah2-mediated degradation of Dcc, we co-expressed Siah2 with Dcc fused to pHluorin (Dcc-pH)(Fig. 3B) in HEK293T cells. We also co-expressed Siah2 with a mutant form of Dcc-pH, Dcc-pH NXN, in which the last valine and proline of the Siah degron motif are replaced by two arginines, thereby abrogating Siah degradation<sup>25</sup> (Fig. 3C). Whereas Siah2 decreased the level of Dcc-pH protein, that of Dcc-pH NXN remained unaffected by co-expression with Siah2. Furthermore, immunoprecipitation with an antibody against GFP showed that the K48-linked ubiquitin signal was more abundant when Dcc-pH was co-expressed with Siah2 but was absent when Dcc-pH NXN was co-expressed with Siah2 (Fig. 3D). Therefore, Siah2 degradation of Dcc is a likely mechanism for restricting Dcc expression to CGNs, as these cells lack Siah2 expression.

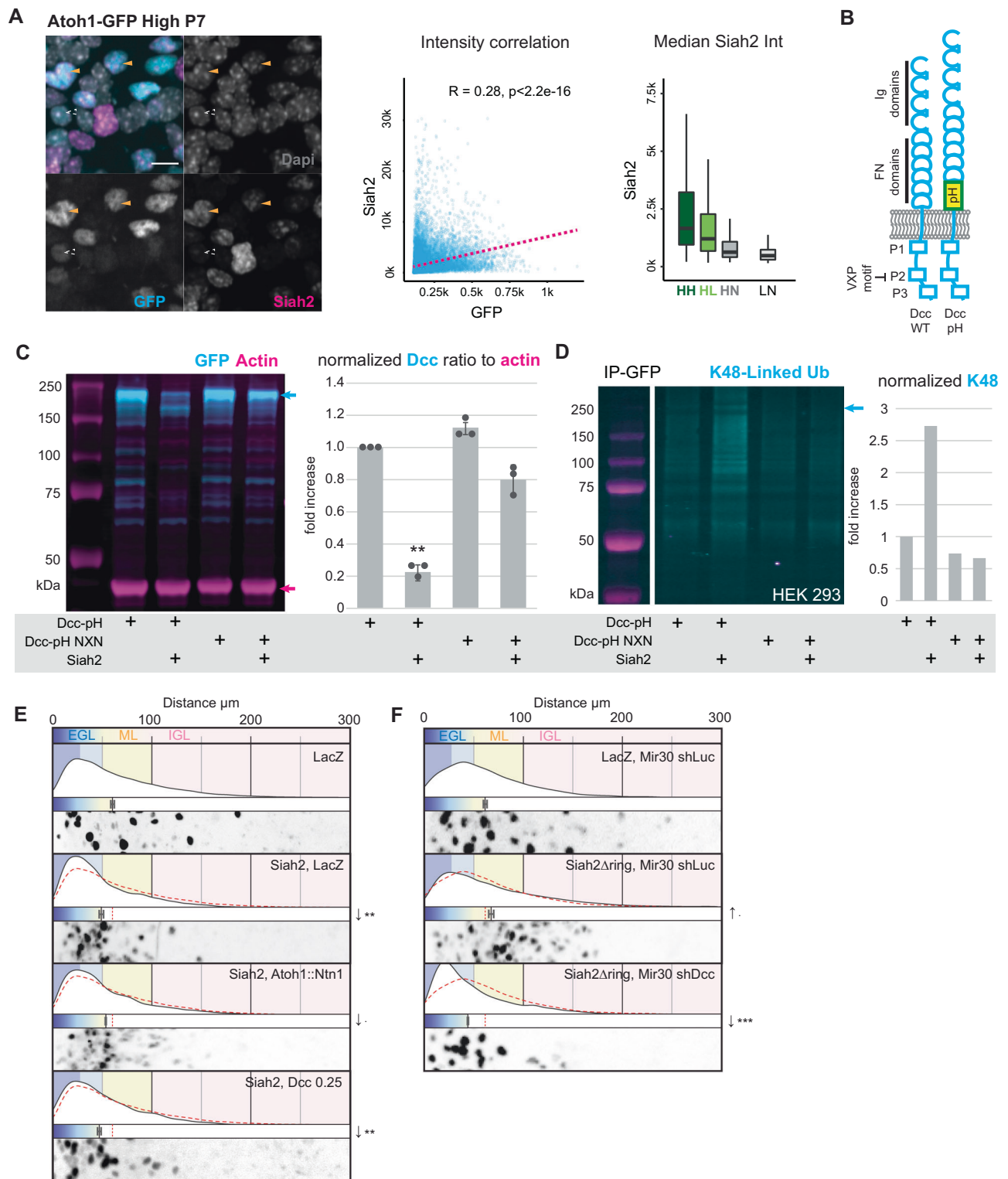
Next, we assessed whether Siah2 regulation of Dcc protein levels was relevant to CGN GZ exit by conducting epistasis analysis in our ex vivo cerebellar slice and microslide assays. Elevated Siah2 expression inhibited enhanced GZ exit that was elicited by Ntn1 and Dcc gain of function, showing that Siah2 antagonizes Dcc function in GZ exit (Fig. 3E). Indeed, Dcc silencing inhibited the boost in GZ exit that is elicited by overexpression of a dominant-negative form of Siah2 lacking the Ring domain (Siah2 $\Delta$ RING)<sup>6,17</sup>, showing that the additional GZ exit that accompanies Siah2 inhibition relies on Dcc function, as would be expected from the Siah2–Dcc antagonism (Fig. 3F). These results suggest that Siah2 expression in GNPs actively hampers GZ exit by targeting Dcc for degradation.

Our previous work showed that Siah2 regulates GZ exit by acting as a negative regulator of partitioning defective (Pard) cell polarity pathways that promote GZ exit. Given that Dcc has been described as a neuronal polarity inducer<sup>26</sup> that, according to our findings, regulates GZ exit and is also negatively regulated by Siah2, we were curious whether there was a relation between the Pard complex and Dcc. Partitioning deficient protein 3 (Pard3) also contains the Siah2 degron motif, and the proteasomal degradation of the latter prevents Pard3

from recruiting JamC to the cell membrane surface, with the result that CGNs accumulate in the GZ<sup>6</sup>.

JamC is a single pass transmembrane protein containing 2 Ig domains that can form homophilic interactions in Cis and Trans<sup>6</sup>. While Dcc requires specific ligand binding, it has also been recently described in forming cis and trans homophilic interactions<sup>27</sup>. To test whether Dcc interacted in a complex with JamC, we expressed these proteins in HEK293T cells and showed that JamC-Halo was present in the pull-down when Dcc-pHluorin was immunoprecipitated with an anti-GFP antibody (Fig. 4A). The JamC–Dcc interaction required the Dcc extracellular domain, as JamC was able to pull-down the extracellular domain of Dcc but not the intracellular domain alone (Fig. S4A). Dcc-pHluorin could also pull down Pard3-Halo (Fig. S4B), but we were less confident about this interaction because Pard3-Halo showed periodic binding to the immunoprecipitation beads. Immunocytochemical staining of dissociated CGNs plated on laminin revealed areas in which the Dcc signal overlapped with the signal for Pard3 or JamC or both (Figure S4C). We designed fusion proteins carrying reporters to enable us to image all three proteins in live neurons with super-resolution. CGNs expressing Dcc-pHluorin, JamC-SNAP (stained with LAMPshade magenta<sup>28</sup>), and Halo-Pard3 were imaged with an Airyscan microscope, which has approximately 100 nm XY resolution. The pHluorin fluorescent protein fused to Dcc and the LAMPshade magenta dye that stained JamC-SNAP shares a pH-dependent fluorescence such that we imaged only the population of Dcc and JamC that was exocytosed to the extracellular face of the plasma membrane, which has a neutral pH when compared to the interior of a vesicle. When expressed together, the Dcc signal overlapped with that of JamC at the cell surface in locations where cells formed the point of contact with other cells in large, bright adhesion plaques (Fig. 4C, D; Fig. S4D). Whereas the JamC signal appeared stable, Dcc was more dynamic in the middle of the JamC domain and coalesced at the edge of some JamC-labeled adhesions (Movie S1). The DCC signal sometimes coincided with the underlying Pard3 signal in fast-moving retrograde or stable Dcc clusters (Fig. 4C, D; Fig. S4E; Movie S2). When Dcc, JamC, and Pard3 were co-expressed together, Pard3 accumulated below the large plaque of JamC that also overlapped with a brighter Dcc signal (Fig. 4C, white arrowhead). It is important to note that Dcc did not localize exclusively to JamC/Pard3 structures and was distributed as a diffuse signal or in a clustered (brighter) structure at the membrane surface. Bright Dcc clusters often accumulated around a JamC/Pard3 bright adhesion between two cells (Fig. 4D, hollow arrowhead). After Ntn1 was added to the medium, Dcc aggregated in clusters (Fig. 4D, cyan arrowhead), some of which were recruited to JamC/Pard3 plaques (Fig. 4D, hollow arrowhead).

As Dcc coincidence with JamC and Pard3 appears to involve a subset of the total Dcc pool within the cell, we assessed their proximity in situ using the Duolink<sup>®</sup> proximity labelling assay<sup>29</sup>. We used a pair of



antibodies targeting the respective extracellular domains (ECD) of Dcc and JamC and a pair of antibodies targeting the intracellular domain (ICD) of Dcc and Pard3. While negative control only showed minimal background, the proximity labeling assay was positive between the Dcc and JamC ECD, as well as Dcc ICD and Pard3, demonstrating a ~40 nm proximity between the polarity proteins and Dcc guidance receptor<sup>29</sup>. Regardless, the proximity of Dcc, JamC, and Pard3 in CGNs and the interactions detected in immunoprecipitation experiments suggest that Dcc forms a complex with polarity-related proteins such as JamC and Pard3.

Next, we conducted epistasis experiments to test whether Pard3 and JamC proteins influenced the effect of Ntn1 on GZ exit through Dcc in an ex vivo slice assay. Knockdown of both *Pard3* and *JamC* mRNA was previously reported to prevent radial migration of CGNs and GZ exit<sup>6</sup> (Fig. 5A). Overexpression of Ntn1 in the GZ or mild expression of Dcc stimulated GZ exit in Pard3-silenced cells, meaning that the loss of Pard3 could be rescued by increasing the Ntn1 signaling (Fig. 5A). In contrast, the phenotype observed with loss of JamC could not be rescued by overexpression of Ntn1, and mild overexpression of Dcc only restored GZ exit to the control level (Fig. 5A). We then tested

**Fig. 3 | Siah2 catalyzes K48 DCC ubiquitination while DCC-Siah2 antagonism regulates GZ occupancy and sensitivity to recombinant Ntn1.**

**A** Immunocytochemistry of Atoh1-GFP FACS-sorted CGNs from P7 mouse cerebellum, cultured for 24 h. Cells were stained for GFP (cyan), Siah2 (magenta), and Dapi (gray). Left graph demonstrates a significant Pearson correlation ( $R = 0.28$ ,  $H_0: t = 46.231$ ,  $df = 24956$ ,  $p$ -value  $< 2.2e-16$ ) between GFP and Siah2 intensity in segmented cell bodies. Boxplot shows distribution of Siah2 intensity, median value represented as a line within a box extending to the first and third quartile and “whiskers” extending to the minimum and maximum values (excluding outliers), across four populations: HH, HL, HN, and LN defined in Fig. 2. **B** Dcc protein schematic showing the four Ig domains, six FN domains, and three intracellular regions (P1, P2, P3). The canonical Siah2 degron motif (VXP) is located within P2. A modified version, Dcc-pH, includes a pH-sensitive GFP inserted between the transmembrane and FN domains. **C** Western blot of HEK293T cells transfected with Dcc-pHluorin (Ctrl), Dcc-pH NXN mutant, and Siah2. The blot was probed with antibodies against GFP (cyan) and actin (magenta). Graph shows the Dcc/actin ratio

normalized to the control ( $n = 3$ ). **D** Western blot of GFP-IP from HEK293 cells transfected with Dcc-pH, Dcc-pH NXN mutant, and Siah2, treated with proteasome inhibitor MG132. The blot was probed for K48-linked ubiquitin (cyan). Arrow indicates the absence of K48-ubiquitin in the Dcc-pH NXN mutant. The graph shows normalized K48-ubiquitin intensity ( $n = 1$ ). **E, F** Ex vivo slice culture assays showing radial distribution of H2B-positive electroporated nuclei. Plots represent distance of nuclei from the slice edge, with average radial distance indicated. Micrographs show nuclear distribution under different conditions. **E** Constructs used include LacZ (control,  $n = 5$ ), Siah2 ( $n = 3$ ), Siah2 + Atoh1::Ntn1 ( $n = 3$ ), and Siah2 + Dcc ( $n = 3$ ). **F** Constructs include LacZ and Mir30 shLuc (control,  $n = 4$ ), Siah2 $\Delta$ ring + Mir30 shLuc ( $n = 4$ ), and Siah2 $\Delta$ ring + Mir30 shDcc ( $n = 3$ ). Scale bar in (A) = 50  $\mu$ m. Abbreviations: EGL external granule layer, ML molecular layer, IGL internal granule layer. Error bars represent SEM. Statistics:  $p \leq 0.1$ ,  $*p \leq 0.05$ ,  $**p \leq 0.01$ ,  $***p \leq 0.005$ , via Student's  $t$ -test (two-sided, unpaired) (C) or ANOVA followed by Dunnett post-hoc test (E, F). See Source Data File.

whether the *Dcc* mRNA knockdown phenotype could be rescued by overexpression of *Pard3* or *JamC*. *Pard3* expression that promoted GZ exit also rescued knocked-down *Dcc*, restoring the level to that in the controls, and *JamC* expression rescued migration, restoring it to that seen in the control group (Fig. 5B). In channel microslide assays, overexpression of both *Pard3* and *JamC* in an unsorted population of dissociated CGNs plated on laminin led to a switch in the migratory response from attraction to repulsion to a source of *Ntn1* (Fig. 5C), whereas knockdown of the mRNA left the cellular migration unbiased to the *Ntn1* source (Fig. 5C). These results suggest that *Pard3* and *JamC* contribute to how CGNs integrate *Ntn1* signaling through *Dcc*, as their levels affect the outcome of cellular migration and are necessary for generating an oriented GZ repulsion migratory response (Fig. 5C). This suggests that *Pard3* and *JamC* synergize with *Dcc* to integrate the *Ntn1* signal that guides CGNs out of the GZ as they differentiate. The ability of elevated *Ntn1* levels to rescue the *Pard3* phenotype implies that *Dcc* signaling deficits in *Pard3*-deficient cells can be compensated by boosting the *Ntn1* signal. In addition, the upregulation of *Dcc* alone was sufficient to rescue the *Pard3* LOF phenotype, further confirming its critical role in compensating for the loss of *Pard3*.

To test the hypothesis that *Dcc* availability was regulated by the expression of *Siah2* in GNP or *Pard3* and *JamC* in differentiated CGNs, we used Dcc-pHluorin as a reporter for *Dcc* at the membrane surface and measured the clustering of *Dcc* in response to *Ntn1* being added to the culture medium<sup>30,31</sup>. The ratio of the segmented clustered area to the total cell area was calculated over time before and after the addition of *Ntn1* (Fig. 6B). In the controls cells expressing LacZ, bright *Dcc* clusters rapidly appeared on the cell surface (Fig. 6A, arrowhead), resulting in the clustered area fraction increasing minutes after the addition of *Ntn1* (Fig. 6C, blue) before slowly returning to normal. Overexpression of *Siah2* resulted in a strong decrease in *Dcc* at the cell surface, whereas both *JamC* and *Pard3* expression were associated with an increased baseline presence of *Dcc* at the cell surface (Figs. 6C, D). Under all conditions, adding *Ntn1* increased the clustered *Dcc* membrane fraction with *Pard3* levels being significantly higher than in the controls (Fig. 6D). Knockdown of *Siah2* resulted in a slight increase in *Dcc* at the membrane at rest, although this was not significant, and the increased clustered area after *Ntn1* addition appeared to decay faster than in the control situation (Fig. 6E–G). Knockdown of either *Pard3* or *JamC* strongly reduced the amount of *Dcc* presented at the cell surface and the amount that was triggered after the addition of *Ntn1* (Fig. 6E–G). Interestingly, *Pard3* overexpression could rescue the knockdown of *JamC* phenotype on membrane-exposed *Dcc* at rest and after *Ntn1* addition (Fig. S5A, B), suggesting that *Pard3* and *JamC* might act through additional pathways to promote *Dcc* membrane recruitment or stabilization. *JamC* specifically appears to have a role in spatially anchoring *Dcc* clusters, as they see their mobility reduced (Blue

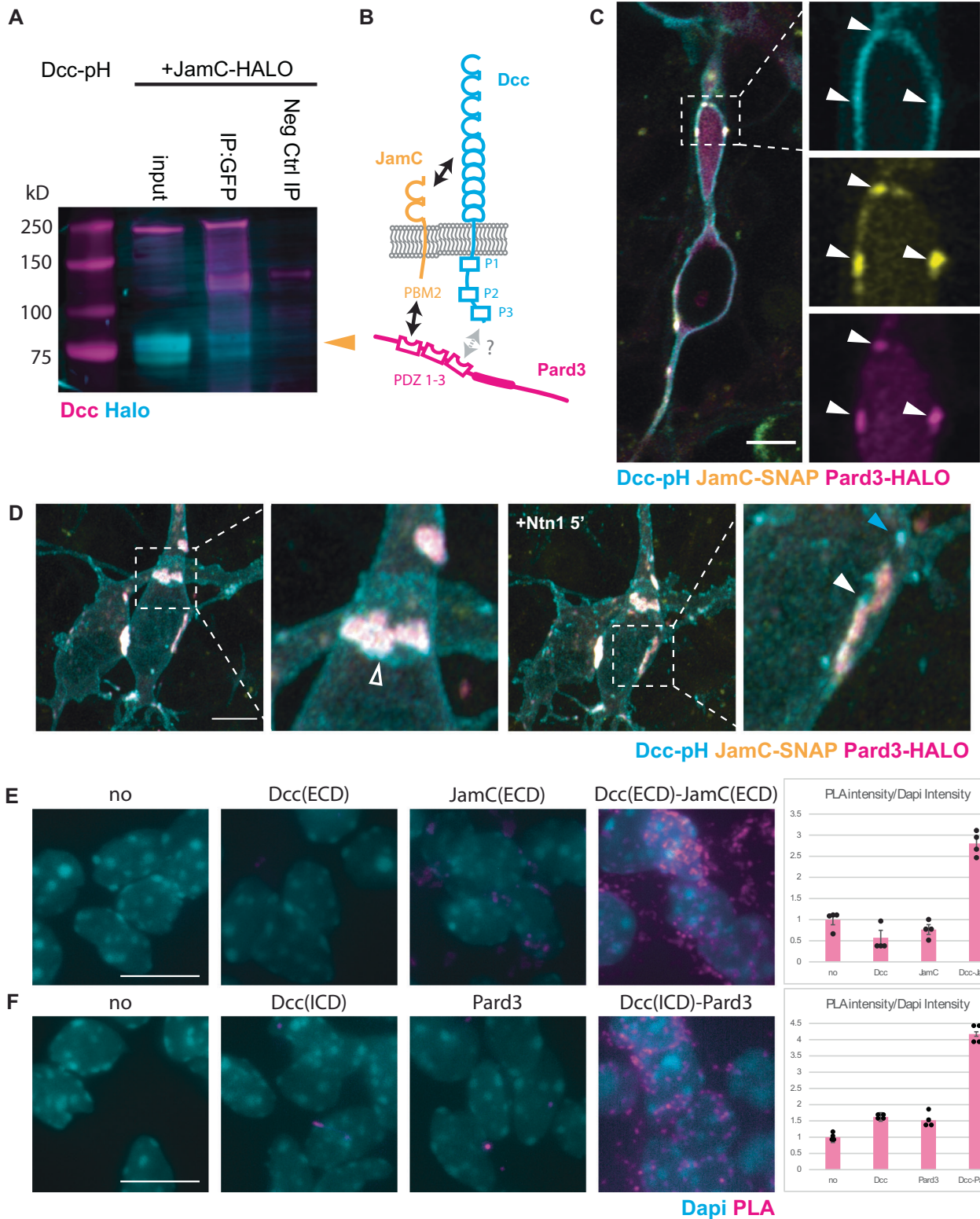
arrowheads, Fig. S5C), which is disrupted with the expression of the dominant negative *JamC* cytoplasmic domain protein (Movie S3)<sup>32</sup>. Moreover, *JamC* dominant negative construct expression also reduces the Dcc-pHluorin signal in *Dcc* puncta after *Ntn1* addition. Overall, these results indicate that the amount of *Dcc* presented at the cell surface is influenced by the cell polarity pathway and the *JamC* adhesion molecule.

Guided by questions about whether *Dcc* clustering could be affected by differentiation status, we expanded our studies to investigate the surface distribution of endogenous *Dcc* in CGNs through their differentiation process using live immunocytochemistry on sorted populations from dissociated CGNs from Atoh1-GFP knock-in mice (Fig. S6A, B). Using random forest 3D segmentation, the total volume of *Dcc* puncta at the membrane surface was measured for individual cells, then sorted by their Atoh1 Nuclear GFP intensity as a differentiation status indicator. The average *Dcc* puncta/cluster size population distribution was also assessed. Results show that the total membrane *Dcc* amount increases as progenitor (HH) differentiates into neurons (HM and HL) and eventually decreases as neurons continue to differentiate (HN and LN). Progenitors exhibit diffuse and smaller *Dcc* structures, while differentiated neurons have bigger aggregates localized more specifically at branching points and neurite tips (Fig. S6A, B). Consistent with our Dcc-pHluorin experiments, *Pard3* and *JamC* expression increased endogenous *Dcc* at the cell surface (Fig. S6D–F).

## Discussion

In the developing nervous system, progenitor GZ occupancy and subsequent postmitotic neuron migration are traditionally viewed as distinct neuronal maturation phases. Failing to recognize the coordination between these stages and the differential impact of extrinsic cues at specific developmental time points may cause us to overlook critical mechanisms that regulate the timing and sequence of maturation within a lineage, resulting in an incomplete understanding of neural development. While GZ exit and radial migration mark the transition from progenitor proliferation to terminal neuronal differentiation, how ‘station keeping’ between cells in these two states is communicated and interpreted at the cell biological level remains unknown. For example, increased cell adhesion can sort cells that share complementary profiles between layers in a developing nervous system tissue by increased cell adhesion molecule expression; however, this sorting is a deterministic event that requires little to no communication between the cells in each layer. In this study, we used the GZ exit of differentiating CGNs of the cerebellum as a model to study how extracellular guidance cue receptors, cellular polarity complexes, and adhesion proteins can intersect, creating a coincidence detection circuit that modulates cell migration behaviors (Fig. 7).





We found that Ntn1 signaling affects the somal translocation direction of CGNs. Interestingly, we observed a gradual shift in Ntn1-dependent migratory behaviors; GNP are unresponsive to this signal, which ultimately transitions to one, causing CGNs to be repulsed by a source of Ntn1 as these cells terminally differentiate and mature. Although Ntn1 has previously been described as having a repulsive effect on the migratory behavior of postmitotic neurons<sup>33,34</sup>, this is definitive example of a transitional guidance behavior for the same lineage based on the differentiation status of the cells and a change of

substrate. It is critical to note that GNPs themselves produce the Ntn1 protein repulsive to the CGN progeny of this progenitor population. Thus, the unresponsiveness of GNPs to the Ntn1 signal from the GZ, while CGNs respond to it, creates the critical station-keeping event that separates these cells in the inner and outer EGL via differential migratory behaviors. Interestingly, most neuronal GZ cells in the developing nervous system express Ntn1 during their peak of proliferation, like what is seen in the ventricular zone of the spinal cord and the ganglionic eminence<sup>34,35</sup>. This suggests that acquiring Ntn1

**Fig. 4 | DCC, Pard3 and JamC are in close proximity to CGN adhesions.**

**A** Western blot of HEK293T cell lysates transfected with Dcc-pHluorin (Dcc-pH) and JamC-HALO. Immunoprecipitation was performed using GFP or negative control IgG antibodies. Blots were probed for Dcc and HALO-tag, with the yellow arrowhead indicating the expected JamC-HALO band size. **B** Schematic depicting interactions between Dcc, JamC, and the polarity protein Pard3. Pard3 recruits JamC to the membrane through its PDZ1 domain, which binds the Class 2 PDZ motif at JamC's C-terminus. JamC interacts with Dcc's extracellular domain, while Pard3's PDZ3 the PDZ 3 domain is predicted to interact with a Class 1 PDZ binding motif (X-S/T-X- $\Phi_{\text{COOH}}$ )<sup>31,52</sup>, present on Dcc intracellular domain. **C, D** Airyscan confocal imaging of CGNs nucleofected with Dcc-pHluorin (cyan), JamC-SNAP (yellow), and Halo-Pard3 (magenta). Phluorin and the SNAP dye used here are both pH sensitive highlighting membrane-bound proteins. **C** Single focal plane showing overlap of Dcc with JamC and Pard3 at the proximal dilation of a CGN (white arrowheads). **D** Maximum projection of two CGNs forming an adhesion, showing Dcc clustering

at the adhesion site before and after Ntn1 addition (200 ng/L). Dcc co-localized with JamC/Pard3 at the adhesion (white arrowhead) and accumulated at the adhesion periphery (hollow arrowhead). Five minutes after the addition of Ntn1 at 200 ng/L, the number of bright Dcc clusters (blue arrowhead) at the membrane surface increased and some newly formed clusters were recruited to the periphery of the JamC/Pard3/Dcc-positive adhesion (white arrowhead). Proximity Labelling Assay (PLA) using Duolink™ fluorescence protocol on fixed dissociated granule neurons plated on laminin and cultured for 24 h, using 2 pairs of primary antibodies: Rabbit against Dcc extracellular domain (ECD) and a Goat against JamC ECD (**E**), and Mouse against Dcc intracellular domain (ICD) and a Rabbit against Pard3 (**F**). Duolink™ staining with no primary, only one or both primaries were compared. Bar graphs represent the ratio of PLA staining intensity (Gray) against Dapi (Cyan) intensity normalized to the negative control without primary antibody (E:  $n = 4$ , F:  $n = 4$ ), replicated 4 (E) and 3 (F) times with similar results. Scale bars: (C, D) 5  $\mu\text{m}$ , (E-F) 10  $\mu\text{m}$ . Error bars represent SEM. See Source Data File.

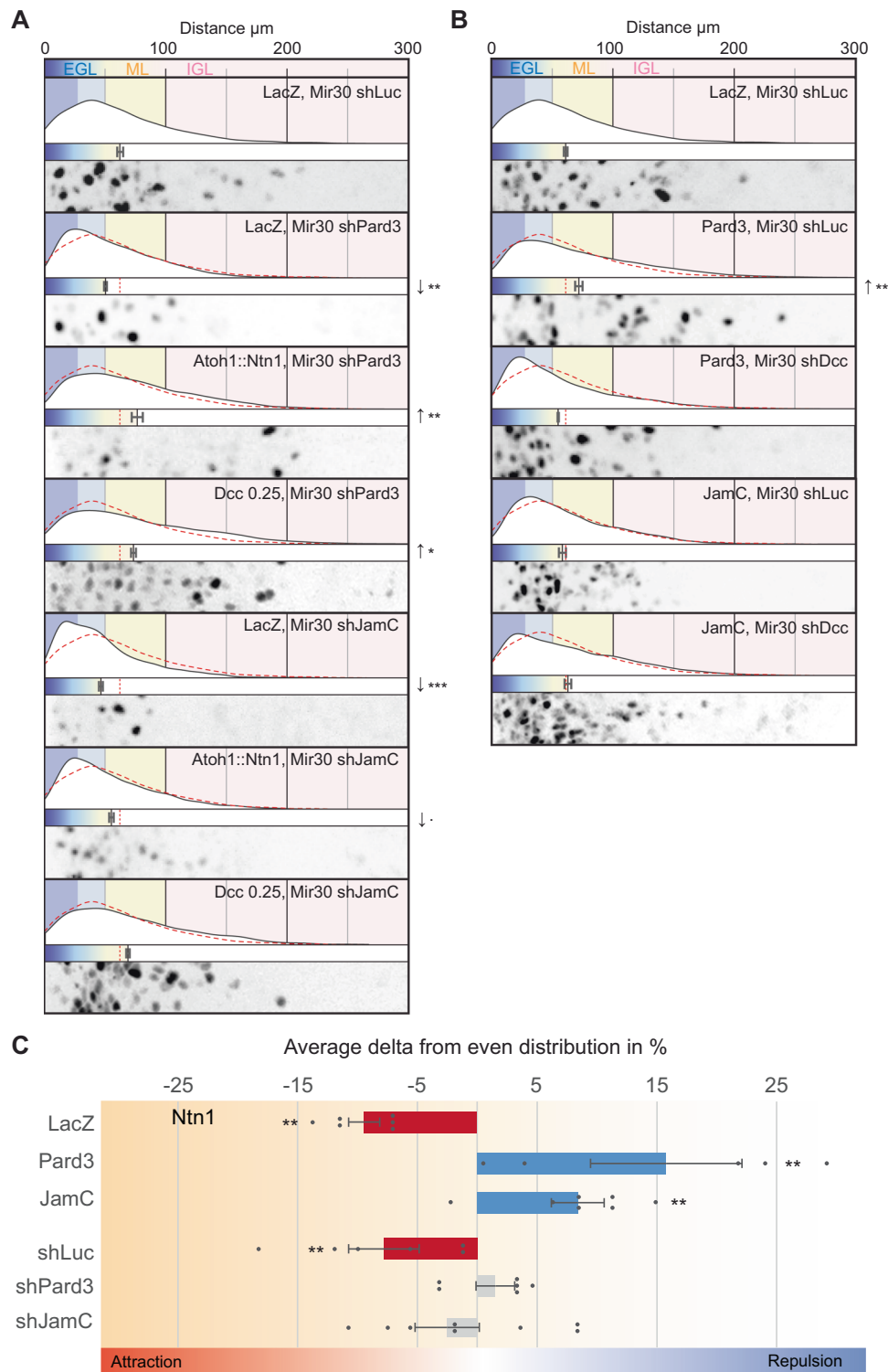
directional sensitivity by newborn neurons as they differentiate could be a common mechanism to prevent the cells from migrating or projecting back into other GZs<sup>33,36</sup>.

How is Ntn1 sensitivity ensured during CGN differentiation? We uncovered a coincidence detection circuit whereby JamC and Pard3 are required for Ntn1-induced GZ exit because of the ability of these proteins to increase basal levels of the Dcc receptor at the plasma membrane and to increase Ntn1-induced Dcc exocytosis. Although many signaling pathways have been characterized as transducing Dcc signaling in response to Ntn1, this mechanism ultimately controls the level of CGN repulsion via Ntn1 by affecting the number and distribution of signal receptors at the cell surface. Previous results from our laboratory have shown that Pard3 causes JamC exocytosis only in differentiated CGNs, which is required for GZ exit. In this study, we have expanded on these results to show that Dcc and JamC extracellular domains interact. Moreover, super-resolution Airyscan microscopy revealed that a subset of Dcc receptors localizes to the periphery of JamC adhesion plaques and that Dcc exocytosis after Ntn1 addition occurs near JamC adhesion plaques. Thus, we have provided functional evidence that Pard3 and JamC cooperate with Dcc to promote GZ exit, and the effect of adding Dcc at JamC adhesions suggests a coincidence detection mechanism whereby engaged adhesion receptors at the cell surface provide a template for adding more Dcc. The polarity protein Pard3 also positively affects the amount of Dcc at the cell surface. However, it is unclear whether this results from a direct action promoting Dcc exocytosis and/or stabilization of large Dcc aggregates at the membrane surface. The connection between Dcc and the Pard3–JamC polarity-dependent adhesion pathway that creates neuronal adhesion during GZ exit is intriguing. Dcc has been noted to create cell polarity events, including effects on axon formation, and directed invasions of cells in development<sup>26,36–38</sup>; however, no connection between Dcc and the core polarity pathways has previously been described. Cell migrations frequently require oscillatory mechanisms in cytoskeletal organization or receptor recruitment that are stabilized by cell polarity pathways<sup>37,39</sup>. The coincidence detection circuit between Pard complexes and JamC adhesions promotes such oscillatory stabilization: In unmanipulated CGNs, Dcc receptors are quickly cleared from the cell surface after bath application of Ntn1, whereas the clearance of Dcc receptors is enhanced by Pard3/JamC loss of function and delayed by Pard3/JamC gain of function. Differentials of Dcc receptors stabilization and subsequent activity at the cell surface coincident with Pard3/JamC localization promote CGNs cell bodies to exit its GZ, which is essentially a directionally polarized behavior. It will be of great interest to understand how this GZ circuit is precisely controlled at the subcellular level: Although the CGN soma migrates in an Ntn1/Dcc-dependent fashion towards the IGL, CGN parallel fiber axons and their growth cones maintain their position in the molecular layer even in the presence of Ntn1.

While Ntn1 response is often studied in the growth cone of developing neurons, we also demonstrate that control of Dcc levels

and access to the membrane is key to regulating the exit of CGN soma from the EGL. Here, we have confirmed that Dcc is a Siah2 target and have shown that Ntn1-dependent GZ exit can be restrained in GNPs through targeted proteasomal degradation of Dcc by Siah2. Interestingly, Siah2 frequently targets multiple components of particular cell biological processes for degradation<sup>24</sup>. This appears to be the case for the Ntn1–Dcc GZ exit pathway, as Siah2 also targets Pard3 for degradation, which positively regulates Dcc membrane occupancy. Siah2 expression in GNPs can restrain Ntn1-induced GZ exit by directly targeting Dcc or factors that promote Dcc membrane occupancy. By equally promoting Pard3 degradation and, therefore, inhibiting JamC access to the cell surface<sup>6</sup>, Siah2 acts as a master regulator of Ntn1 sensitivity in GNPs. Determining whether Siah2 has further roles in modulating Dcc will be interesting, as previous studies have shown that Ntn1 can promote Dcc ubiquitination<sup>40</sup>. Indeed, given the rapid disappearance of surface Dcc after Ntn1 addition, Siah2 activity may be regulated by Ntn1 activity, or Siah2 affinity for Dcc may be modified due to Ntn1 binding. It is worth noting that another ubiquitin ligase, Trim9, also regulates Dcc clustering. Trim9 loss of function compromises Dcc clustering, but the loss of clustering is related to unrestrained exocytosis of a host of cargos controlled by soluble N-ethylmaleimide attachment protein receptor (SNARE) proteins due to focal adhesion kinase activation<sup>41</sup>. Interestingly, Siah2 degrades Trim9; it may be interesting to dissect whether this additional ubiquitin ligase is part of a larger ubiquitin ligase circuit regulating Dcc signaling in cooperation with Siah2.

We demonstrate that Unc5c, a prototypical Dcc co-receptor, is necessary and sufficient for CGN GZ exit. While Unc5 homologs are traditionally known to convert Dcc–Ntn1 responses from attraction to repulsion, particularly in growth cones<sup>15</sup>, their role in neuronal migration in mouse models is more nuanced. Earlier studies suggested that Unc5 homologs negatively regulate neuronal migration. For example, increased Unc5b expression in Sip1 mutants reduces cortical interneuron migration into the developing cerebral cortex<sup>42</sup>. Yamagishi et al. and Seiradake et al. also showed that downregulation of Unc5d, in response to FLRT receptors, is required for cortical neurons to leave the intermediate zone and move to the cortical plate, while elevated Unc5d expression slows this migration<sup>43,44</sup>. In contrast, Akkermans et al. proposed that newborn cortical neurons are repelled from ventricular zone radial glia due to a trans-recognition of Glypican-3 and Unc5d, which is partly analogous to the oEGL repulsion we report here<sup>45</sup>. Our finding that elevated Unc5c expression converts attraction to repulsion aligns with the classical role of this co-receptor pair. However, the differentiation-specific expression of Unc5c introduces the following concept: differentiation status and the continuum of differentiation states can significantly alter a cell lineage's Ntn1 responsiveness. In this case, a complex interplay of polarity proteins, adhesion molecules, and Unc5c. How does Pard3 or JamC GOF promote repulsion? Our model that involves receptor stabilization and



differentiation status inputs suggests two interpretations that are not mutually exclusive. In the first simple scenario, increased Pard3 and JamC can increase Dcc surface occupancy in maturing CGNs already experiencing higher Unc5c expression levels, thus promoting repulsion. Indeed, our observation that a mild elevation in Dcc induces repulsion supports the notion that higher surface Dcc is sufficient to trigger this response in cerebellar slices. In the second scenario, it's also possible that Pard3 GOF can promote CGN differentiation directly, which could favor the CGN-differentiation-specific expression of Unc5c. Interestingly, a recent modeling study by Limerick et al. suggested that *C. elegans* Unc5 unexpectedly regulates asymmetric

Unc40 localization, the worm Dcc ortholog; however, no connections were made in this model to classic polarity proteins<sup>46</sup>. Our results suggest that given Pard proteins cooperate with Dcc, an ancient polarity-inducing receptor, the cerebellar system may also provide an opportunity to uncover Pard-Unc5 connections related to Dcc clustering and membrane asymmetry.

The differential responsiveness of the CGN lineage to Ntn1 contrasts sharply with other contexts where cell-intrinsic states modulate Ntn1 responses. For instance, Moo-Ming Poo's lab showed that calcium transients from non-selective cation channels can rapidly alter nerve growth cone responses to Ntn1, independent of

**Fig. 5 | DCC, Pard3 and JamC epistatically regulate GZ occupancy and CGN sensitivity to recombinant Ntn1.** **A, B** Results of ex vivo slice culture assays under different conditions. In each case, the top curve shows the entire distribution of the radial distances of H2B-positive electroporated nuclei from the edge of the slice in replicates. Below this is a plot of the average radial distance from the edge among replicates, and below this is a micrograph representative of the nuclear distribution after 48 h in culture. All are displayed on the same scale, representing a distance from 0 to 300  $\mu\text{m}$ . In addition to H2B-Cherry, the following constructs were electroporated: in **(A)**, LacZ+Mir30 shLuc (control,  $n = 5$ ); LacZ+Mir30 shPard3 ( $n = 4$ ); Atoh1::Ntn1+Mir30 shPard3 ( $n = 4$ ); Dcc at 0.25  $\mu\text{g}$ +Mir30 shPard3(4); LacZ+Mir30 shJamC ( $n = 5$ ); Atoh1::Ntn1+Mir30 shJamC ( $n = 5$ ); and Dcc at 0.25  $\mu\text{g}$ +Mir30 shJamC ( $n = 3$ ); in **(B)**, LacZ+Mir30 shLuc (control,  $n = 5$ ); Pard3+Mir30 shLuc ( $n = 6$ ); Pard3+Mir30 shDcc ( $n = 4$ ); JamC+Mir30 shLuc ( $n = 3$ ); and JamC+Mir30 shDcc ( $n = 4$ ). Each respective control is represented by a red dashed line in the distribution plot. **C** Chart representing the average variation

across replicates in the endpoint nuclear displacement on the x-axis from an even probability of 50%:50%, with negative values representing an attraction to the source of the Ntn1 gradient (in red when statistically significant) and positive values representing repulsion (in blue when statistically significant). Unsorted dissociated CGNs were nucleofected and plated on laminin-coated channel microslides for 24 h, then Ntn1 was added unilaterally into the channel 10 min before the start of nuclear tracking for 2 h. Cells were nucleofected with H2B-mCherry, GPI-pHluorin, and the following: LacZ (control,  $n = 6$ ), Pard3 ( $n = 5$ ), JamC ( $n = 7$ ), Mir30 shLuc (control,  $n = 6$ ), Mir30 shPard3 ( $n = 8$ ), and Mir30 shJamC ( $n = 6$ ). Abbreviations: EGL external granule layer, ML molecular layer, IGL internal granule layer. In **(A)** through **(C)**, error bars represent the SEM. Statistics:  $p \leq 0.1$ ,  $*p \leq 0.05$ ,  $**p \leq 0.01$ ,  $***p \leq 0.005$ , as assessed by an ANOVA followed by a Dunnett post hoc test against the respective controls in **(A)** and **(B)** and by a chi-square test in **(C)** against an even probability of 50%:50%. See Source Data File.

fate changes<sup>47</sup>. Similarly, in spinal cord motor axons, Unc5c and EphrinB2 create an integrative guidance response between Ntn1 and ephrins, guiding medial LMC axons<sup>48</sup>. This synergy may be driven by differential transcriptional gene expression during lateral or medial LMC specification<sup>49</sup>, yet differentiation status was not assessed. Our work uncovers a distinct mechanism by which differentiating neurons exit the GZ, emphasizing the role of cell polarity in modulating the interaction between adhesive signals and Netrin-1. Unlike models focused on rapid growth cone behavior changes or fate-defined axon guidance, our work reveals how cell polarity and adhesion proteins create a coordinated circuit that regulates Netrin-1 receptor availability. This circuit effectively gates the repulsion needed for GZ exit and initiates radial migration through differentiation-driven changes in cell biology, impacting surface levels of Dcc. The increased expression of Unc5c and Pard3 during the GNP to CGN transition, coupled with the more effective JamC adhesion in CGNs that regulates Ntn1 responsiveness through Dcc, highlights this transition as a pivotal step toward terminal differentiation. Siah-mediated degradation of Pard3 and Dcc in GNPs illustrates how the progenitor state actively represses these CGN-specific events, reinforcing the differentiation switch in Ntn1 sensitivity and the coincidence detection circuit. While Dcc, an ancient polarity-inducing molecule, has been studied extensively, our work connects Dcc to a classical cell polarity signaling cascade, specifically linking it to Pard3. This connection integrates Dcc into established polarity mechanisms, revealing how polarity signaling drives terminal differentiation. It allows differentiating neurons to navigate complex niche environments, effectively aligning their trajectory with a defined differentiation path while overcoming the challenges of integrating multiple extrinsic cues during germinal zone exit.

## Methods

### Mice

All mouse lines were maintained in standard conditions (e.g., pathogen-free and with continuous access to food/water) in accordance with guidelines established and approved by the Institutional Animal Care and Use Committee at St. Jude Children's Research Hospital (Protocol no. 483). B6.129(SJL)-Ntn1tm1.1Tek/J, Tg(Atoh1-cre/Esr1\*)14Fsh/J, B6.Cg-Gt(ROSA)26Sortm9(CAG-tdTomato)Hze/J, B6.129S-Atoh1tm4.1Hzo/J, and C57BL/6J mouse strains were obtained from The Jackson Laboratory. Neonates were collected on postnatal days 7 through 9 for the studies detailed in the Methods section below or as indicated in the experimental details in the figures. Male and female mice were mixed for the described experiments as no effect of sex on the timing of GZ exit or migration initiation has been observed so far in scientific literature.

### Method details

Blinding was not used in data collection.

### Plasmid vectors

Expression plasmids for LacZ, Pard3a, Siah2, Siah2 $\Delta$ RING, and H2B-mCherry were subcloned as previously described<sup>6,7</sup> pCIG2 Dcc-pHluorin (Dcc-pH), with a pH-sensitive form of green fluorescent protein (GFP)<sup>50</sup> inserted in position 1090, was obtained from Franck Polleux at Columbia University. All new cDNA constructs encoded mouse (*mus musculus*) proteins and were cloned in the laboratory by the overlapping PCR method. See the Supplementary Data 1 File, for a complete recombinant DNA list.

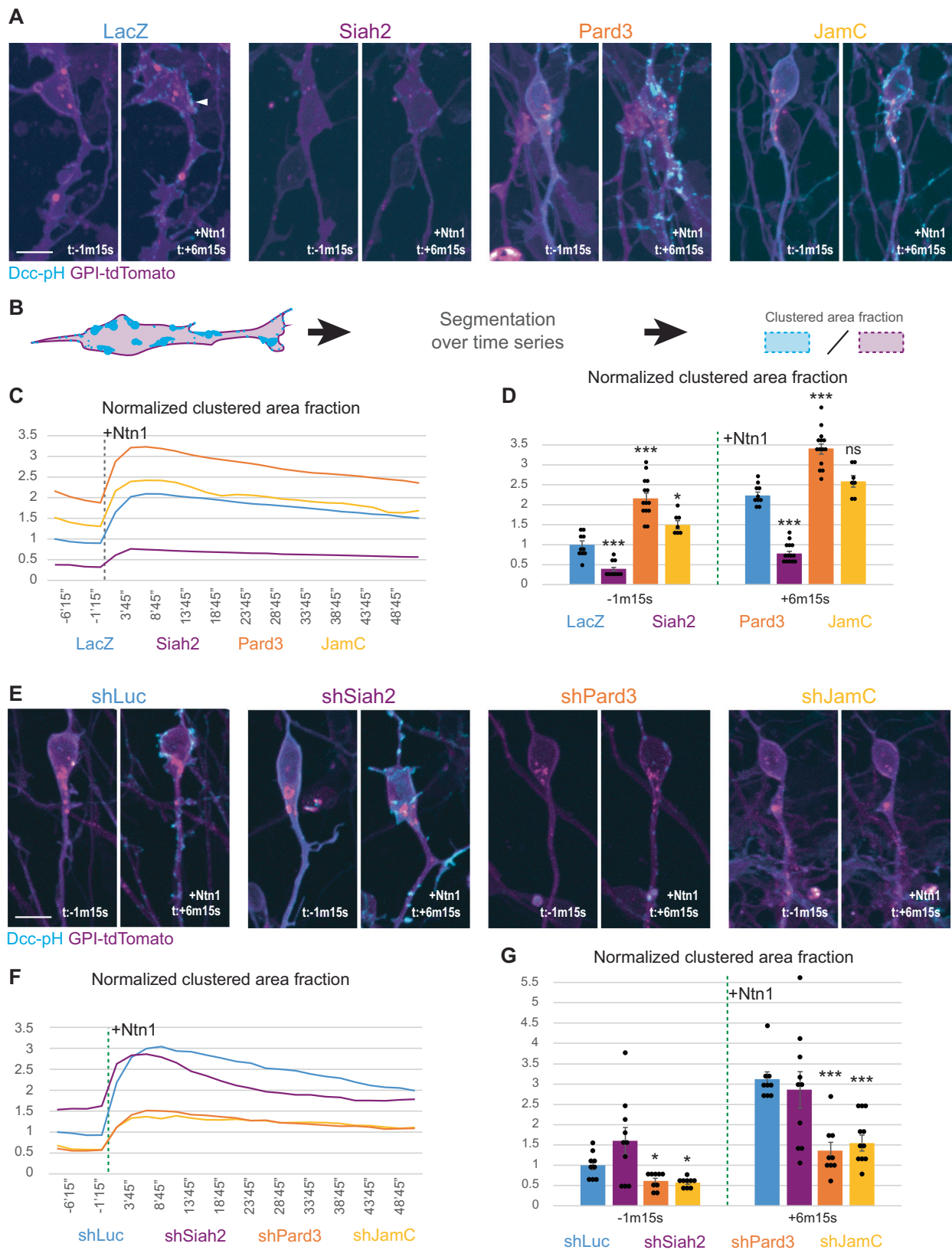
### Western blot analysis

Mycoplasma free HEK293T cells (ATCC) were lipofected (using Lipofectamin 2000; Thermo Fisher Scientific) 1 day before being harvested. Cells were lysed using Lysis/Binding/Wash Buffer (Cell Signaling Technologies) with Halt™ Protease and Phosphatase Inhibitor Cocktail (Thermo Fisher Scientific) and reduced using Laemmli buffer (Sigma-Aldrich, cat. no. S3401). Samples were subjected to polyacrylamide gel electrophoresis using the Bolt™ system (Thermo Fisher Scientific) and transferred to PVDF membranes (Immobilon®-FL PVDF Membrane), blocked in Intercept blocking Buffer, and immunoblotted with appropriate antibodies (see the Supplementary Data 1 file for dilutions). For immunoprecipitation and co-immunoprecipitation experiments, the Protein G Immunoprecipitation Kit was used with 1  $\mu\text{g}$  of anti-GFP antibody (RRID: AB\_221569) or control IgG (RRID: AB\_2722735) per the manufacturer's protocol. Samples were then blotted as previously described. HEK293T cells used for blot analysis of the K48-linked ubiquitin signal (RRID:AB\_10859893, 1:1000 dil) were treated for 6 h with the proteasome and calpain inhibitor MG132 (50  $\mu\text{M}$ ) before being subjected to lysis to see the ubiquitin mark.

### Ex vivo cerebellar electroporation, organotypic slice culture imaging

Cerebella of P7 WT (C57BL/6J) mice were dissected, and the superficial layer of the meninges was removed. Cerebella were soaked in endotoxin-free plasmid DNA suspended in Hank's balanced salt solution (1–3  $\mu\text{g}/\mu\text{L}$  of each DNA was generally used, with pCIG2-mCherryH2B being electroporated as a nuclear marker for migrating CGNs), transferred to a CUY520-P5 platinum-block Petri dish electrode (Protech International), and electroporated with a CUY21EDIT square-wave electroporator (90 V, 5 pulses, 50-ms pulse, 500 ms interval) (Protech International). Electroporated cerebella were embedded in 4% low-melting-point agarose, and 300  $\mu\text{m}$  sagittal cerebellar slices were prepared using a VT1200 Vibratome (Leica Microsystems). Slices were transferred to Millicell tissue culture inserts (Millipore) and incubated in serum-free medium (FluoroBrite™ DMEM supplemented with 2 mM L-glutamine, 50 cU/mL penicillin–streptomycin, and 1  $\times$  B27 and 1  $\times$  N2 supplements [Gibco]).

To measure the migration distance of CGNs, cerebellar slices were fixed with 4% paraformaldehyde, mounted on slides using ProLong



Gold (Invitrogen), and imaged at 20 $\times$  with a spinning-disk confocal microscope. Measurements were made with the Amira software, using a self-written script for detecting local maxima of H2B-mCherry-positive nuclei and a Euclidian transform giving the distance from the cerebellar pial surface. Statistical analysis were performed, and graphs were prepared with RStudio software.

### Spinning disk confocal microscope

Imaging was performed using a Marianas Spinning Disk confocal microscope (Intelligent Imaging Innovations), which includes a Zeiss Axio Observer microscope with the following objectives:  $\times 40/1.0$  NA Plan-Apochromat (oil immersion),  $\times 63/1.4$  NA Plan-Apochromat (oil immersion), and  $\times 40$  C-Apochromat 1.2 W Corr M27

**Fig. 6 | Siah2 antagonizes while Pard3/JamC promotes DCC clustering and exocytosis as a mechanism regulating Ntn1 responsiveness.** **A, E** Spinning-disk confocal live-cell imaging of dissociated granule neurons plated on laminin for 24 h after nucleofection with Dcc-pHlorin (Dcc-pH) (cyan), GPI-TdTomato (magenta), and one of the following: in (A), LacZ (Ctrl,  $n = 10$ ), Siah2 ( $n = 14$ ), Pard3 ( $n = 14$ ) or JamC ( $n = 7$ ); in (E), Mir30 shLuc (Ctrl,  $n = 9$ ), Mir30 shSiah2 ( $n = 10$ ), Mir30 shPard3 ( $n = 9$ ), or Mir30 shJamC ( $n = 9$ ). Cells were tracked for a total of 1 h at 150 s intervals. Representative pictures for each condition show a maximum projection before ( $t = -1$  m 15 s) and after ( $t = +6$  m 15 s) the addition of Ntn1 at 200 ng/mL. **B** Schematic representing the segmentation process for the analysis of the time-lapse images in (A) and (E). The Dcc-pH and GPI-TdTomato channels were segmented using Pixel classification with Ilastik. The resulting “clustered area fraction” is the ratio of the

area of the segmented Dcc-pH regions (bright Dcc clusters) to the area of the membrane in each field of view for each time point. **C, F** Graphs representing the Dcc-pH area fraction over the membrane area, normalized to their respective controls. The different experimental conditions are the same as those in (A) and (E). A dashed-line marks the addition of 200 ng/mL of Ntn1 at  $t_0$ . **D, G** Bar charts highlighting data presented in (C) and (F) for a time point before the addition of Ntn1 ( $t = -1$  m 15 s) and for another time point shortly thereafter ( $t = +6$  m 15 s). In **D, G** error bars represent the SEM. Statistics: ns, non-significant,  $*p \leq 0.05$ ,  $**p \leq 0.01$ ,  $***p \leq 0.005$ , as assessed by an ANOVA followed by a Games–Howell post hoc test against the respective controls. See also Source Data File. Scale bars in (A) and (E) represent 10  $\mu\text{m}$ .

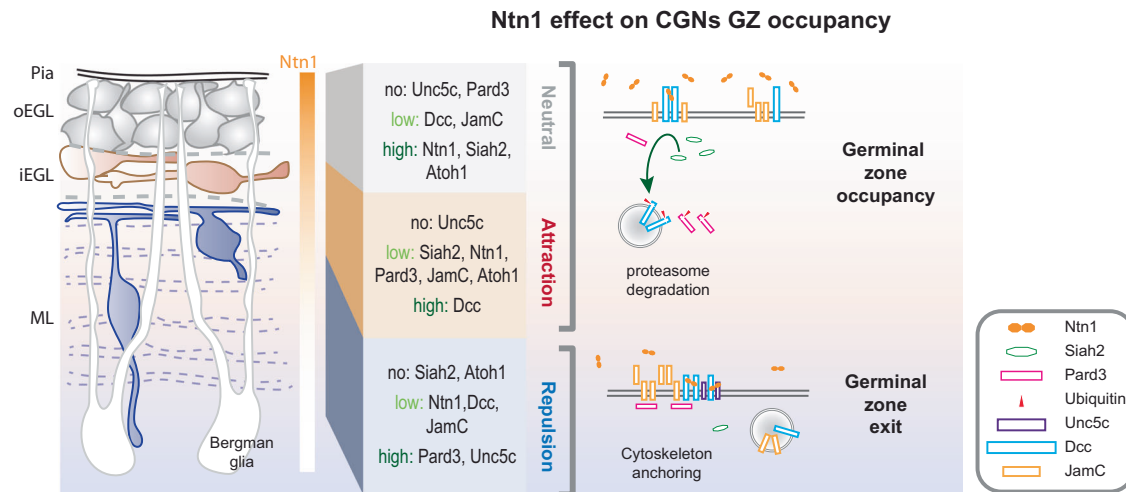


**Fig. 7 | Model for the adhesion-guidance coincidence circuit.** The left panel shows the various stages of CGNs and their relative layer occupancy (gray = GNPs, peach = newly differentiated CGN, blue = maturing CGN). The right panel shows the layer-specific response to Netrin-1 produced in the GZ. Siah2 degrades Dcc and Pard3 in GNPs rendering them unresponsive to Netrin-1. Newly differentiated CGNs

are slightly attracted to Netrin-1, likely controlling how long these cells remain in the iEGL. Maturing CGNs express high levels of Pard3 which promotes exocytosis of JamC and Dcc and formation of larger structures at the membrane surface. The need of JamC adhesion for Dcc to exit the germinal zone in response to Netrin-1 is at the heart of the coincidence detection circuit.

(WD = 0.14–0.28 mm). The system had an Ultraview CSUX1 confocal head and 440–514 nm or 488–561 nm excitation filters. An ImageEM-intensified CCD camera (Hamamatsu) was used for high-resolution imaging. Video recordings were captured using Slidebook software (Intelligent Imaging Innovations).

### Preparation and nucleofection of CGNs

Briefly, cerebella were dissected from the brains of P7 WT (C57BL/6J) mice, then the tissue was coarsely chopped and treated with a Neural Tissue Dissociation Kit (Miltenyi Biotec). The suspension was layered onto a discontinuous Percoll gradient (35% and 60%) and separated by centrifugation. Cells at the 35%–60% interface were isolated. The resulting cultures routinely contained >95% CGNs and <5% glia. Plasmid expression vectors encoding proteins of interest were introduced into granule neurons via Amaxa nucleofection, using an Amaxa Mouse Neuron Nucleofector Kit in accordance with the manufacturer’s instructions and program O-005. The concentration of pCIG2 expression vectors used for each construct (5 to 25  $\mu\text{g}$  of DNA per 6 million cells) was determined empirically but was consistent across replicates. After cells had been allowed to recover from the nucleofection for 10 min, they were plated in appropriate culture chambers and maintained in culture for 24 h in serum-free medium. For analysis of the Dcc clustering response to Ntn1 (Fig. 6), immunocytochemistry (Figs. S2B, S4B), and live imaging (Fig. 4A–C; Fig. S4C, D), we used 6-cm dishes with glass bottoms that had been treated with poly-L-ornithine then coated with laminin at 1  $\mu\text{g}/\text{cm}^2$ .

### Atoh1-eGFP-sorted cells

Mouse pups homozygous for *Atoh1::GFP* (B6.129S-Atoh1tm4.1Hzo/J; The Jackson Laboratory, JAX: 013593) were collected at P7, and cerebellar granule neurons were isolated after dissociation by the methods described above. “High” and “low” populations were sorted, based on their GFP intensity, with a cell sorter (FACSaria Fusion, BD Biosciences; 85  $\mu\text{m}$  nozzle, 35 PSI). The GFP intensity distribution profile was constant (Fig. S2A), and the gating criteria were consistent across replicates.

### Migration assays on channel microslides

For migration assays, microslides ( $\mu$ -Slide I; Ibidi, cat. no. 80106) were treated with poly-L-ornithine and then coated with laminin at 1  $\mu\text{g}/\text{cm}^2$  or vitronectin at 2  $\mu\text{g}/\text{cm}^2$ . Two million nucleofected CGNs or freshly sorted “low” or “high” *Atoh1::GFP* cells (prepared as described above) were then added to the channel and left to incubate. After 24 h, before the start of the time-lapse image acquisition, the medium was replaced twice by aspirating the existing medium from one end of the track and adding 100  $\mu\text{L}$  of warm, fresh medium at the other end. After a 10 min incubation, the same procedure was repeated, but this time adding only 50  $\mu\text{L}$  of serum-free medium containing Ntn1 to a final concentration of 200 ng/mL or the equivalent volume of 1  $\times$  PBS as a control. Cells were then tracked every 150 s for 130 min after Ntn1 addition in a spinning-disk confocal microscope with environmental control. Cell body migration was tracked manually with SlideBook (Intelligent Imaging Innovations) by

using the H2B-mCherry signal (in nucleofected cells) or differential interference contrast (DIC) (in Atoh1-sorted cells). Cells showing less than 10  $\mu\text{m}$  of total displacement over the time-lapse period were analyzed.

### Cerebellar immunohistochemistry

Postnatal brains were fixed by immersion in 4% paraformaldehyde at 4 °C overnight, washed five times in 1 $\times$  PBS for 24 h, and then cryoprotected in PBS containing 30% sucrose. Histologic sagittal sections were cut on a cryostat and pre-blocked for 1 h in PBS with 0.2 M glycine, 0.1% Triton X-100, and 10% normal donkey serum. Sections were incubated overnight at 4 °C with the primary antibodies (see the Supplementary Data 1 file for list of antibodies and dilutions). This was followed by incubation at room temperature for 1 h with the appropriate Alexa Fluor-labeled secondary antibody (Invitrogen; diluted 1:1000) before mounting. Images were acquired with a spinning-disk microscope using SlideBook software.

### Proximity labelling assay

Proximity labelling assay was carried out using Duolink<sup>®</sup> system (Sigma-Aldrich), following the manufacturer instructions and recommended controls, on dissociated CGNs plated on laminin and cultured at 37 °C for 24 h after fixation 2% PFA/0.5% Glutaraldehyde. Two pairs of primary antibodies were used: Rabbit against Dcc (ECD) (ab273570, Abcam 1:200 dil) and Goat against JamC (ECD) (AF1213, R&D systems, 1:50 dil), and Mouse against Dcc (ICD) (A-1, Santa Cruz 1:100 dil) and Rabbit against Pard3 (07-330, Sigma-Aldrich 1:200 dil).

### Pulse-chase assay in Atoh1::CreERT2; Ntn1<sup>flox/flox</sup>

Tamoxifen in corn oil was injected intraperitoneally (at 100 mg/kg body weight) at P0, P1, and P2. For pulse-chase migration assays, mice were injected intraperitoneally with 50 mg/kg of EdU 48 h before tissue collection. EdU incorporation was assayed with the Click-iT assay (Invitrogen) according to the manufacturer's instructions.

### Quantification and statistical analysis

Standard image processing and analysis were done with Amira (Thermo Fisher), SlideBook, or Fiji software. For cluster area analysis, pixels were classified with a random forest classifier, using Ilastik for sum projection after drift and Fiji for photobleach correction. Analyzed metrics of quantitated data are expressed as the mean  $\pm$  SEM or as an adjusted ratio of clustering relative to the control average at the initial time point. The Student *t*-test was used to compare two groups. A one-way analysis of variance (ANOVA) was used for multiple comparisons with the Dunnett post hoc test against controls (for ex vivo slices) or with the Games–Howell post hoc test (for cluster area analysis). A non-parametric post hoc test was used for the cluster area analysis because the data did not satisfy the homogeneity of variance. The chi-square test was used in the channel microslide migration assay to test the results against an even probability (0.5) of the relative endpoint displacement on the axis of the length of the channel being either toward or away from the source of the gradient. In this assay, data were expressed graphically as the percentage variation from 50%, showing the mean  $\pm$  SEM across replicates. All statistical test assumptions were verified when required by the test.

### Reporting summary

Further information on research design is available in the Nature Portfolio Reporting Summary linked to this article.

### Data availability

All the plasmids generated in this study and the detailed sequences will be available on request from the corresponding author R.F. Requests will be processed in 1–2 weeks. Source data are provided with this paper.

## References

- Hatten, M. E. Central Nervous System Neuronal Migration. *Annu. Rev. Neurosci.* **22**, 511–539 (1999).
- Hakanen, J., Ruiz-Reig, N. & Tissir, F. Linking Cell Polarity to Cortical Development and Malformations. *Front Cell Neurosci.* **13**, 244 (2019).
- Chedotal, A. Should I stay or should I go? Becoming a granule cell. *Trends Neurosci.* **33**, 163–172 (2010).
- Hatten, M. E. & Roussel, M. F. Development and cancer of the cerebellum. *Trends Neurosci.* **34**, 134–142 (2011).
- Leto, K. et al. Consensus Paper: Cerebellar Development. *Cerebellum* **15**, 789–828 (2015).
- Famulski, J. K. et al. Siah regulation of Pard3A controls neuronal cell adhesion during germinal zone exit. *Science* **330**, 1834–1838 (2010).
- Singh, S. et al. Zeb1 controls neuron differentiation and germinal zone exit by a mesenchymal-epithelial-like transition. *Elife* **5** (2016).
- Kullmann, J. A. et al. Oxygen Tension and the VHL-Hif1 $\alpha$  Pathway Determine Onset of Neuronal Polarization and Cerebellar Germinal Zone Exit. *Neuron* **106**, 607–623 e5 (2020).
- Laumonerie, C. & Solecki, D. J. Regulation of Polarity Protein Levels in the Developing Central Nervous System. *J. Mol. Biol.* **430**, 3472–3480 (2018).
- Butts, T., Green, M. J. & Wingate, R. J. T. Development of the cerebellum: simple steps to make a 'little brain'. *Development* **141**, 4031–4041 (2014).
- Hallada, L. P., Shirinifard, A. & Solecki, D. J. Junctional Adhesion Molecule (JAM)-C recruitment of Pard3 and drebrin to cell contacts initiates neuron-glia recognition and layer-specific cell sorting in developing cerebella. *eLife*. **13**, RP98384 (2024).
- Ackerman, S. L. et al. The mouse rostral cerebellar malformation gene encodes an UNC-5-like protein. *Nature* **386**, 838–842 (1997).
- Przyborski, S. A., Knowles, B. B. & Ackerman, S. L. Embryonic phenotype of Unc5h3 mutant mice suggests chemorepulsion during the formation of the rostral cerebellar boundary. *Development* **125**, 41–50 (1998).
- Purohit, A. A. et al. Down syndrome cell adhesion molecule (DSCAM) associates with uncoordinated-5C (UNC5C) in netrin-1-mediated growth cone collapse. *J. Biol. Chem.* **287**, 27126–27138 (2012).
- Moore, S. W., Tessier-Lavigne, M. & Kennedy, T. E. Netrins and Their receptors. In *Axon Growth and Guidance* (ed. Bagnard, D.) **621**, 17–31 (Springer, New York, NY, 2007).
- Alcantara, S. et al. Netrin 1 acts as an attractive or as a repulsive cue for distinct migrating neurons during the development of the cerebellar system. *Development* **127**, 1359–1372 (2000).
- Hu, G. & Fearon, E. R. Siah-1 N-terminal RING domain is required for proteolysis function, and C-terminal sequences regulate oligomerization and binding to target proteins. *Mol. Cell Biol.* **19**, 724–732 (1999).
- Hu, G. et al. Mammalian homologs of seven in absentia regulate DCC via the ubiquitin-proteasome pathway. *Genes Dev.* **11**, 2701–2714 (1997).
- Li, Q. et al. Central role of SIAH inhibition in DCC-dependent cardioprotection provoked by netrin-1/NO. *Proc. Natl. Acad. Sci. USA* **112**, 899–904 (2015).
- Mazelin, L. et al. Netrin-1 controls colorectal tumorigenesis by regulating apoptosis. *Nature* **431**, 80–84 (2004).
- Xu, K. et al. Structures of netrin-1 bound to two receptors provide insight into its axon guidance mechanism. *Science* **344**, 1275–1279 (2014).
- Pons, S. et al. Vitronectin regulates Sonic hedgehog activity during cerebellum development through CREB phosphorylation. *Development* **128**, 1481–1492 (2001).
- Ong, T. et al. Siah2 integrates mitogenic and extracellular matrix signals linking neuronal progenitor ciliogenesis with germinal zone occupancy. *Nat. Commun.* **11**, 5312 (2020).

24. Ong, T. & Solecki, D. J. Seven in Absentia E3 Ubiquitin Ligases: Central Regulators of Neural Cell Fate and Neuronal Polarity. *Front Cell Neurosci.* **11**, 322 (2017).
25. House, C. M. et al. A binding motif for Siah ubiquitin ligase. *Proc. Natl. Acad. Sci. USA* **100**, 3101–3106 (2003).
26. Adler, C. E., Fetter, R. D. & Bargmann, C. I. UNC-6/Netrin induces neuronal asymmetry and defines the site of axon formation. *Nat. Neurosci.* **9**, 511–518 (2006).
27. Meijers, R. et al. Netrin Synergizes Signaling and Adhesion through DCC. *Trends Biochem Sci.* **45**, 6–12 (2020).
28. Brown, T. A. et al. Direct detection of SARS-CoV-2 RNA using high-contrast pH-sensitive dyes. *J. Biomol. Tech.* **32**, 121–133 (2021).
29. Alam, M. S. Proximity Ligation Assay (PLA). *Curr. Protoc. Immunol.* **123**, e58 (2018).
30. Matsumoto, H. & Nagashima, M. Netrin-1 elevates the level and induces cluster formation of its receptor DCC at the surface of cortical axon shafts in an exocytosis-dependent manner. *Neurosci. Res.* **67**, 99–107 (2010).
31. Gopal, A. A. et al. Netrin-1-Regulated Distribution of UNC5B and DCC in Live Cells Revealed by TICCS. *Biophys. J.* **110**, 623–634 (2016).
32. Ebnet, K. et al. The cell polarity protein ASIP/PAR-3 directly associates with junctional adhesion molecule (JAM). *EMBO J.* **20**, 3738–3748 (2001).
33. Hamasaki, T. et al. A role of netrin-1 in the formation of the sub-cortical structure striatum: repulsive action on the migration of late-born striatal neurons. *J. Neurosci.* **21**, 4272–4280 (2001).
34. Yamagishi, S., Bando, Y. & Sato, K. Involvement of Netrins and Their Receptors in Neuronal Migration in the Cerebral Cortex. *Front Cell Dev. Biol.* **8**, 590009 (2020).
35. Yung, A. R., Nishitani, A. M. & Goodrich, L. V. Phenotypic analysis of mice completely lacking netrin 1. *Development* **142**, 3686–3691 (2015).
36. Varadarajan, S. G. & Butler, S. J. Netrin1 establishes multiple boundaries for axon growth in the developing spinal cord. *Dev. Biol.* **430**, 177–187 (2017).
37. Wang, Z. et al. UNC-6 (netrin) stabilizes oscillatory clustering of the UNC-40 (DCC) receptor to orient polarity. *J. Cell Biol.* **206**, 619–633 (2014).
38. Dominici, C. et al. Floor-plate-derived netrin-1 is dispensable for commissural axon guidance. *Nature* **545**, 350–354 (2017).
39. Hao, J. C. et al. The tripartite motif protein MADD-2 functions with the receptor UNC-40 (DCC) in Netrin-mediated axon attraction and branching. *Dev. Cell* **18**, 950–960 (2010).
40. Kim, T. H. et al. Netrin induces down-regulation of its receptor, Deleted in Colorectal Cancer, through the ubiquitin-proteasome pathway in the embryonic cortical neuron. *J. Neurochem* **95**, 1–8 (2005).
41. Plooster, M. et al. TRIM9-dependent ubiquitination of DCC constrains kinase signaling, exocytosis, and axon branching. *Mol. Biol. Cell* **28**, 2374–2385 (2017).
42. van den Berghe, V. et al. Directed migration of cortical interneurons depends on the cell-autonomous action of Sip1. *Neuron* **77**, 70–82 (2013).
43. Yamagishi, S. et al. FLRT2 and FLRT3 act as repulsive guidance cues for Unc5-positive neurons. *EMBO J.* **30**, 2920–2933 (2011).
44. Seiradake, E. et al. FLRT structure: balancing repulsion and cell adhesion in cortical and vascular development. *Neuron* **84**, 370–385 (2014).
45. Akkermans, O. et al. GPC3-Unc5 receptor complex structure and role in cell migration. *Cell* **185**, 3931–3949 e26 (2022).
46. Limerick, G. et al. A Statistically-Oriented Asymmetric Localization (SOAL) Model for Neuronal Outgrowth Patterning by *Caenorhabditis elegans* UNC-5 (UNC5) and UNC-40 (DCC) Netrin Receptors. *Genetics* **208**, 245–272 (2018).
47. Wang, G. X. & Poo, M. M. Requirement of TRPC channels in netrin-1-induced chemotropic turning of nerve growth cones. *Nature* **434**, 898–904 (2005).
48. Poliak, S. et al. Synergistic integration of Netrin and ephrin axon guidance signals by spinal motor neurons. *Elife* **4**, (2015)
49. Palmesino, E. et al. Foxp1 and lhx1 coordinate motor neuron migration with axon trajectory choice by gating Reelin signalling. *PLoS Biol.* **8**, e1000446 (2010).
50. Miesenböck, G., De Angelis, D. A. & Rothman, J. E. Visualizing secretion and synaptic transmission with pH-sensitive green fluorescent proteins. *Nature* **394**, 192–195 (1998).
51. Doyle, D. A. et al. Crystal structures of a complexed and peptide-free membrane protein-binding domain: molecular basis of peptide recognition by PDZ. *Cell* **85**, 1067–1076 (1996).
52. Tyler, R. C., Peterson, F. C. & Volkman, B. F. Distal interactions within the par3-VE-cadherin complex. *Biochemistry* **49**, 951–957 (2010).

## Acknowledgements

We thank Franck Polleux for the original Dcc-pHluorin construct and Luke Lavis for sharing the Lampshade Magenta dye. Zeiss 980 Airy Scan images were acquired at the Cell & Tissue Imaging Center Light Microscopy Division (CTIC-LM), supported by SJCRH and NCI P30 CA021765. Drs. Aaron Taylor, Aaron Pitre, and George Campbell provided consultation and support for imaging experiments in the CTIC-LM shared resource at St. Jude. Kim Lowe in DNB's flow sorting core helped produce pure GPNs and CGNs for the study. Keith A. Laycock, Ph.D., ELS, did the scientific editing of the manuscript. The Solecki laboratory is funded by the American Lebanese Syrian Associated Charities (ALSAC) and by grants 1R01NS066936 and R01NS104029 from the National Institute of Neurological Disorders (NINDS). The content of this manuscript is solely the responsibility of the authors and does not necessarily represent the official views of the NIH.

## Author contributions

C.L. designed and carried out all the experiments and analyses. M.S. tracked Atoh1 sorted CGNs and participated in the analysis of Netrin1 in vivo experiments. D.R.S. carried out pilot imaging experiments examining the configuration of surface recruited DCC. T.L.L. constructed the DCC pHluorin construct. N.T. maintained mouse colonies used in all experiments and designed breeding logistics to produce the required animals for all studies. D.H. prepared CGNs, carried out experiment and ensured experimental rigor for pilot experiments. D.J.S. carried out pilot experiments and conceived and supervised the study. All authors drafted or edited the manuscript.

## Competing interests

The authors declare no competing interests.

## Additional information

**Supplementary information** The online version contains supplementary material available at <https://doi.org/10.1038/s41467-024-55400-w>.

**Correspondence** and requests for materials should be addressed to David J. Solecki.

**Peer review information** *Nature Communications* thanks Fabrice Ango, Mikio Hoshino, and the other, anonymous, reviewer for their contribution to the peer review of this work. A peer review file is available.

**Reprints and permissions information** is available at <http://www.nature.com/reprints>

**Publisher's note** Springer Nature remains neutral with regard to jurisdictional claims in published maps and institutional affiliations.



**Open Access** This article is licensed under a Creative Commons Attribution-NonCommercial-NoDerivatives 4.0 International License, which permits any non-commercial use, sharing, distribution and reproduction in any medium or format, as long as you give appropriate credit to the original author(s) and the source, provide a link to the Creative Commons licence, and indicate if you modified the licensed material. You do not have permission under this licence to share adapted material derived from this article or parts of it. The images or other third party material in this article are included in the article's Creative Commons licence, unless indicated otherwise in a credit line to the material. If material is not included in the article's Creative Commons licence and your intended use is not permitted by statutory regulation or exceeds the permitted use, you will need to obtain permission directly from the copyright holder. To view a copy of this licence, visit <http://creativecommons.org/licenses/by-nc-nd/4.0/>.

© The Author(s) 2025